Supporting Information

Ligand-Mediated Proteome Remodeling Dictates Nanoparticle Protein Corona Composition for Deep Plasma Profiling

Bahareh Ghaffari[1,2], Liuchenxin Han[3], Ali Tamadon[4], Alphan Alpaydin[2,5], Ghafar Yerima[4], Nick Wills[1], Shaun Grumelot[2,5], Danilo Ritz[6], Alexander Schmidt[6], Sylvain Peuget[3], Mohammad Ghassemi[7], Hojatollah Vali[8,9], Mohammad R K Mofrad[4], Amir Ata Saei[3*], Babak Borhan[1*], and Morteza Mahmoudi[2,5*]

[1]Department of Chemistry, Michigan State University, East Lansing, Michigan 48824, USA
[2]Precision Health Program, Michigan State University, East Lansing, Michigan 48823, USA
[3]Department of Microbiology, Tumor and Cell Biology, Karolinska Institute, Stockholm 171 77, Sweden
[4]Molecular Cell Biomechanics Laboratory, Departments of Bioengineering and Mechanical Engineering, University of California Berkeley, Berkeley, CA, USA.
[5]Department of Radiology, College of Human Medicine, Michigan State University, East Lansing, Michigan 48823, USA
[6]Proteomics Core Facility, Biozentrum, University of Basel, Basel, Switzerland
[7]Department of Computer Science and Engineering, Michigan State University, East Lansing, Michigan 48824, USA
[8]Department of Anatomy and Cell Biology, McGill University, Montreal, QC, H3A 0C7, Canada
[9]Facility for Electron Microscopy Research, McGill University, Montreal, QC, H3A 0C7, Canada
* AAS (amir.saei@ki.se); BB (babak@chemistry.msu.edu); MM (mahmou22@msu.edu)

Liquid chromatography-tandem mass spectrometry (LC-MS/MS)

Dried peptides were first reconstituted in 0.1% aqueous formic acid (FA) containing 0.02% n-dodecyl-β-D-maltoside (DDM) to ensure optimal solubility and reduce sample loss. Chromatographic separation was achieved using a Vanquish Neo UHPLC system (Thermo Fisher Scientific) coupled to a timsTOF Ultra 2 mass spectrometer (Bruker) via a CaptiveSpray nano-electrospray ion source. Peptides were loaded onto a 30 cm analytical column with a 100 µm internal diameter, packed in-house with ReproSil Saphir 100 C18 resin (1.5 µm particle size; Dr. Maisch GmbH). The column was maintained at a constant temperature of 60°C throughout the run to optimize peak shape and reproducibility.

The separation was performed at a flow rate of 400 nL/min using a binary buffer system consisting of Buffer A (0.1% FA in water) and Buffer B (80% acetonitrile, 0.1% FA in water). The gradient profile was initiated at 2% B, increasing to 25% B over 25 minutes, followed by a ramp to 35% B over 5 minutes. The column was then washed by increasing the organic phase to 95% B over 0.5 minutes, held for 4 minutes, and finally returned to 2% B over 0.5 minutes for a short re-equilibration period.

Mass spectrometry was conducted in data-independent acquisition parallel accumulation-serial fragmentation (dia-PASEF) mode, providing high sensitivity and deep proteome coverage with an estimated cycle time of 0.95 s. Both MS1 and MS2 spectra were acquired over a mass range of 100–1700 m/z. The dia-PASEF scheme employed 8 scans containing 3 ion mobility windows per scan, covering a precursor range of 400–1000 m/z with 25 Da isolation windows. The ion mobility ($1/K_0$) range was set between 0.64 and 1.37 V.s/cm^2. Source parameters were optimized with Ion Charge Control (ICC 2.0) enabled, featuring 100 ms accumulation and ramp times, a 1600 V capillary voltage, 3 L/min dry gas, and a source temperature of 200°C. Collision energy was dynamically adjusted as a linear function of ion mobility, ranging from 59 eV at $1/K_0$ = 1.6 V.s/cm^2 to 20 eV at $1/K_0$ = 0.6 V.s/cm^2.

Data processing was performed using Spectronaut (v19.0, Biognosys) applying the directDIA+ workflow. Raw files were searched against the UniProt *Homo sapiens* reference proteome (downloaded 2022-02-22; 20,360 sequences) and a database of 392 common laboratory contaminants. The search utilized default Spectronaut settings, though Cross-Run Normalization was explicitly disabled to maintain raw quantitative integrity for specific downstream requirements. Final quantitative results were generated and exported using the Pivot Report function for further statistical evaluation.

Data analysis

Raw proteomic datasets were obtained with three replicates per sample. Data processing and analysis were performed using custom Python scripts, and visualization and statistical analyses

were conducted in GraphPad Prism (version 10.6.1). UniProt was used as the reference database for protein identifiers, annotations, and functional classification. Prior to quantitative analysis, contaminant proteins were removed by excluding entries annotated with the prefix "Con–". Missing values were addressed at the replicate level: When a single replicate value was missing (98% of samples contained $\leqslant$4% such instances), the missing value was imputed using the average of the remaining two replicates. Proteins missing values in two replicates were excluded from analysis for that sample, with such cases comprising $\leqslant$0.86% of proteins in every sample. Protein abundances were subsequently normalized to the total protein intensity within each replicate and expressed as relative abundance percentages. These normalized values were used for all downstream analyses to enable compositional comparisons across experimental conditions.

Molecular Dynamics

Preparation

The docked complexes of human serum albumin (HSA) with selected phospholipid-related ligands were prepared for molecular dynamics simulations. To ensure compatibility with the CHARMM36[15] force field, each docked ligand structure was processed using the CHARMM-GUI Ligand Reader and Modeler.[16,17] This step standardized atom names, bonding patterns, and residue identifiers to match the corresponding parameters available in the CHARMM36 force field. Out of all the ligands screened, 3 were not present in the CHARMM36 force field, namely, CDP-coline, benzalkonium chloride, and digitoxin. To obtain their parameters, they were processed through CGenFF program version 4.0[18–20] for similarity-based parameter assignment. Structures with charge and parameter penalty less than or equal to 10 were used as is, namely CDP-coline. The remaining structures were refined via quantum mechanical calculations at the second-order Møller–Plesset perturbation (MP2) level of theory for geometry and bonded parameter optimization and Hartree–Fock for charge optimization using the 6-31G* basis set. FFParam-GUI[21] and Psi4 open-source quantum mechanical calculation program[22] were used to parametrize the ligands. Nevertheless, digitoxin was excluded from the MD simulations due to its unreliable parameters. The corrected ligands were then combined with their respective docked HSA structures to form complete complexes. The resulting structures were converted into GROMACS coordinate and topology files for simulation.

Simulation

All molecular dynamics simulations were carried out using the GROMACS[23] 2022.6 software package with the CHARMM36 force field. The systems were placed in cubic water boxes with a minimal distance from the box edges of 1.5 nm and solvated using the TIP3P water model. Sodium and chloride ions were added to neutralize charge and to reproduce physiological ionic strength at 0.15 M. Each system underwent four stages: energy minimization, temperature equilibration

(NVT), pressure equilibration (NPT), and a production run under constant temperature and pressure. Energy minimization was performed using a steepest descent algorithm with an energy tolerance of 1000 kJ mol^{-1} nm^{-1} for a maximum of 50000 steps at a 0.01 nm step size. Electrostatic interactions used the Particle Mesh Ewald (PME) method with a real-space cutoff of 1.0 nm, and van der Waals interactions were cut at 1.0 nm. Periodic boundary conditions were applied in all three dimensions. Equilibration was performed in two phases: a 1 ns NVT run followed by a 4 ns NPT run using a 1 fs timestep. Temperature was maintained at 310 K and pressure at 1 bar using the Berendsen thermostat and barostat, respectively. Electrostatic interactions were treated with the Particle Mesh Ewald (PME) method and van der Waals interactions with a force-switch cutoff between 1.0 and 1.2 nm. All hydrogen bonds were constrained with the LINCS algorithm. Production simulations were performed for 100 ns under periodic boundary conditions to sample the conformational stability of each HSA-ligand complex in explicit solvent 2 fs timestep using the Parrinello-Rahman barostat. The Verlet cutoff scheme was used for neighbor searching, and coordinates were saved every 10 ps for analysis. All simulations were executed on GPU-accelerated nodes of the SDSC Expanse high-performance computing system.

Analysis

Trajectory analyses were performed to evaluate the dynamic stability and intermolecular interactions of each protein-ligand complex. Root-mean-square deviation (RMSD) and root-mean-square fluctuation (RMSF) were calculated to assess overall structural stability and residue-level flexibility. Hydrogen bonds between the protein and ligand were quantified in terms of number, distance, and lifetime. Short-range nonbonded interaction energies were decomposed into Coulombic (electrostatic) and Lennard-Jones (van der Waals) components and averaged over the simulation trajectories to compare relative binding strengths among systems. Representative structures and interaction patterns were visualized using Visual Molecular Dynamics (VMD) software.[24]

Table S1. Top Binding Affinities for Ligands used in the screening. A higher negative value indicates better binding affinity between the respective ligand and Human Serum Albumin.

Dimer Binding Affinity		
Ligand	**Binding Affinity (kcal/mol)**	**Binding Affinity (kJ/mol)**
Digitoxin	-9.8796	-41.3362464
CDP-Choline (Cytidine Diphosphate Choline)	-7.5074	-31.4109616
Phosphatidic acid (PA)	-6.7943	-28.4273512
Phosphatidylcholine	-6.7311	-28.1629224
Dimyristoylphosphatidylcholine (DMPC)	-6.4049	-26.7981016
Dioleoylphosphatidylcholine (DOPC)	-6.2922	-26.3265648
Dipalmitoylphosphatidylcholine (DPPC)	-5.9308	-24.8144672
Phosphatidylethanolamine (PE)	-5.8137	-24.3245208
Phosphatidylserine (PS)	-5.7283	-23.9672072
Sphingomyelin	-5.6695	-23.721188
Cardiolipin	-5.6325	-23.56638
Lysophosphatidylcholine (LPC)	-5.3573	-22.4149432
Benzalkonium Chloride	-5.322	-22.267248
Acetylcholine	-4.2501	-17.7824184
Choline	-3.6751	-15.3766184
Monomer Binding Affinity		
Ligand	**Binding Affinity (kcal/mol)**	**Binding Affinity (kJ/mol)**
Digitoxin	-10.2357	-42.8261688
Phosphatidic acid (PA)	-7.1578	-29.9482352
Sphingomyelin	-6.794	-28.426096
CDP-Choline (Cytidine Diphosphate Choline)	-6.5014	-27.2018576
Phosphatidylcholine	-6.2227	-26.0357768
Dioleoylphosphatidylcholine (DOPC)	-6.1843	-25.8751112
Dimyristoylphosphatidylcholine (DMPC)	-6.1288	-25.6428992
Phosphatidylethanolamine (PE)	-6.1172	-25.5943648
Phosphatidylserine (PS)	-6.0913	-25.4859992
Dipalmitoylphosphatidylcholine (DPPC)	-6.0736	-25.4119424
Benzalkonium Chloride	-5.8599	-24.5178216
Cardiolipin	-5.3522	-22.3936048
Lysophosphatidylcholine (LPC)	-5.2226	-21.8513584
Acetylcholine	-4.1334	-17.2941456
Choline	-3.7166	-15.5502544

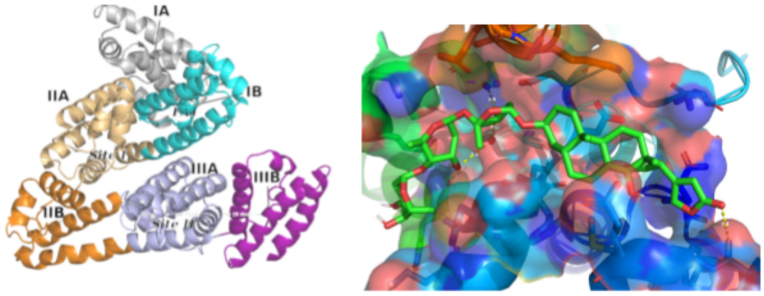

Figure S1. Molecular docking results overview. Left: Overall structure of human serum albumin (HSA, PDB ID: 1AO6) with subdomains IA, IB, IIA, IIB, IIIA, and IIIB labeled. Key binding regions including Sudlow's Site I, Site II, and fatty acid binding site 1 (FA1) are highlighted for spatial context. Right: Binding pose of Digitoxin at the IA/IIIA interface on chain A. This unique site preference demonstrates how steroidal ligands can target inter-domain regions distinct from FA1 and Site I.

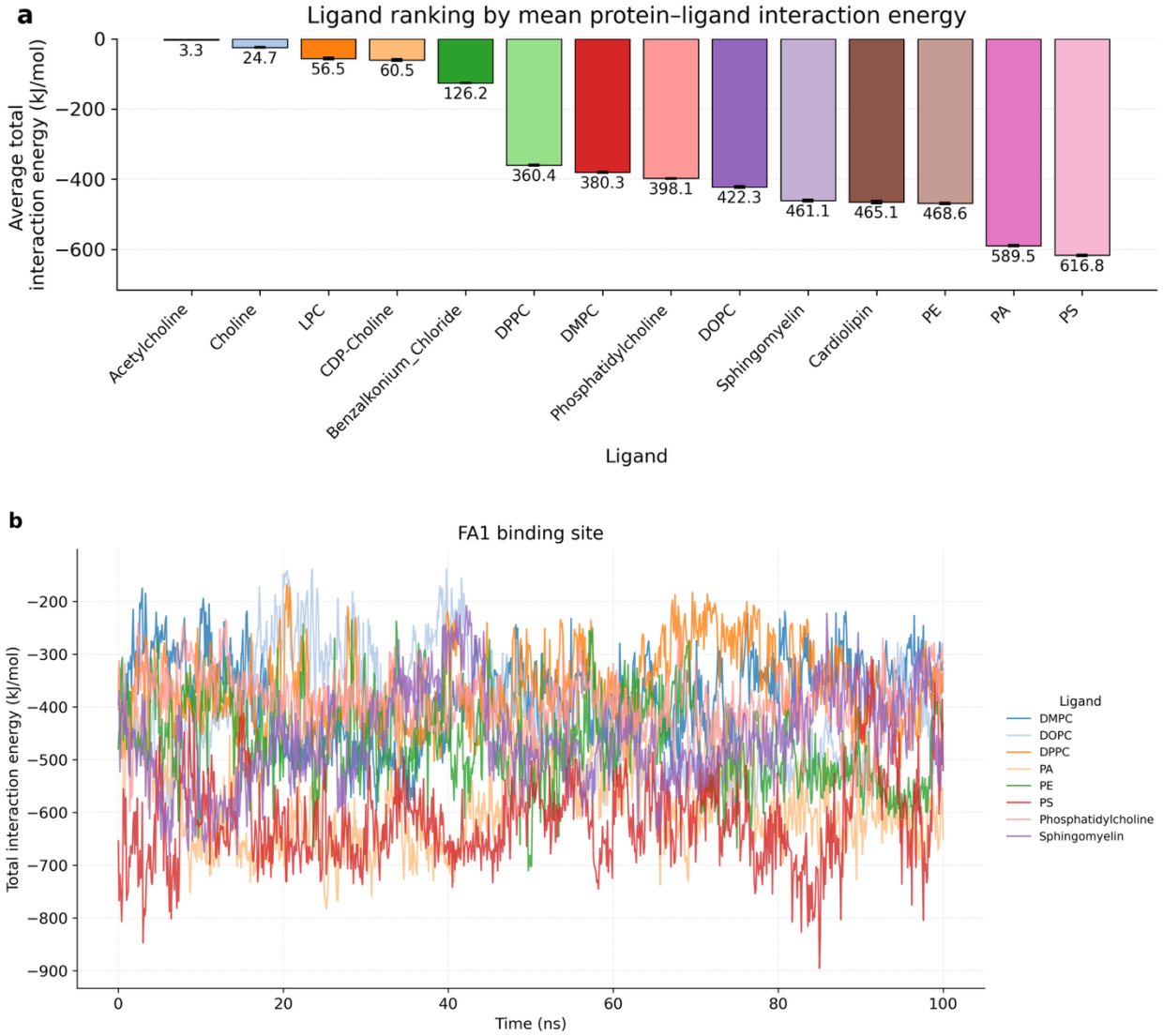

Figure S1. Protein-ligand total interaction energies. (a) Ranking of ligand binding strength to Human Serum Albumin (HSA). Ligands are ranked from left to right corresponding to weakest to strongest binding respectively. Values atop the bars show the Average of the Short-Range Non-Bonded Interaction Energy (Sum of the Coulombic and Lennard-Jones Short-Range Energies) over the 100 ns of simulation timesteps in kJ/mol. Error bars indicate the standard error of the mean. Greater negative values correspond to stronger binding interactions between the protein and ligand. Phosphatidylserine (PS), and Phosphatidic acid (PA) exhibit the strongest binding energies with Acetylcholine, Choline, and Lysophosphatidylcholine (LPC) exhibiting a significantly weak affinity to HSA. (b) Total interaction energies of ligands associated with the Fatty Acid 1 (FA1) binding domain of Human Serum Albumin over the simulation time span. Values of interaction energy obtained from the sum of the Coulombic and Lennard-Jones short-range energies. Time-series points lower in the plot represent instances of high binding affinity of the ligand with the protein HSA. Phosphatidylserine (PS), and Phosphatidic acid (PA) occupy the lower regions of the plot. Dipalmitoylphosphatidylcholine (DPPC), and Dioleoylphosphatidylcholine (DOPC) displayed weaker binding interactions. (c) Total interaction energies of ligands associated with the Sudlow Site I binding domain of Human Serum Albumin over the simulation time span. Values of interaction energy obtained from the sum of the Coulombic and Lennard-Jones short-range energies. Time-series points lower in the plot represent instances of high binding affinity of the ligand with the protein HSA. Cardiolipin binds the strongest to this site. Acetylcholine, Choline, and Lysophosphatidylcholine (LPC) indicated weak to zero association with HSA.

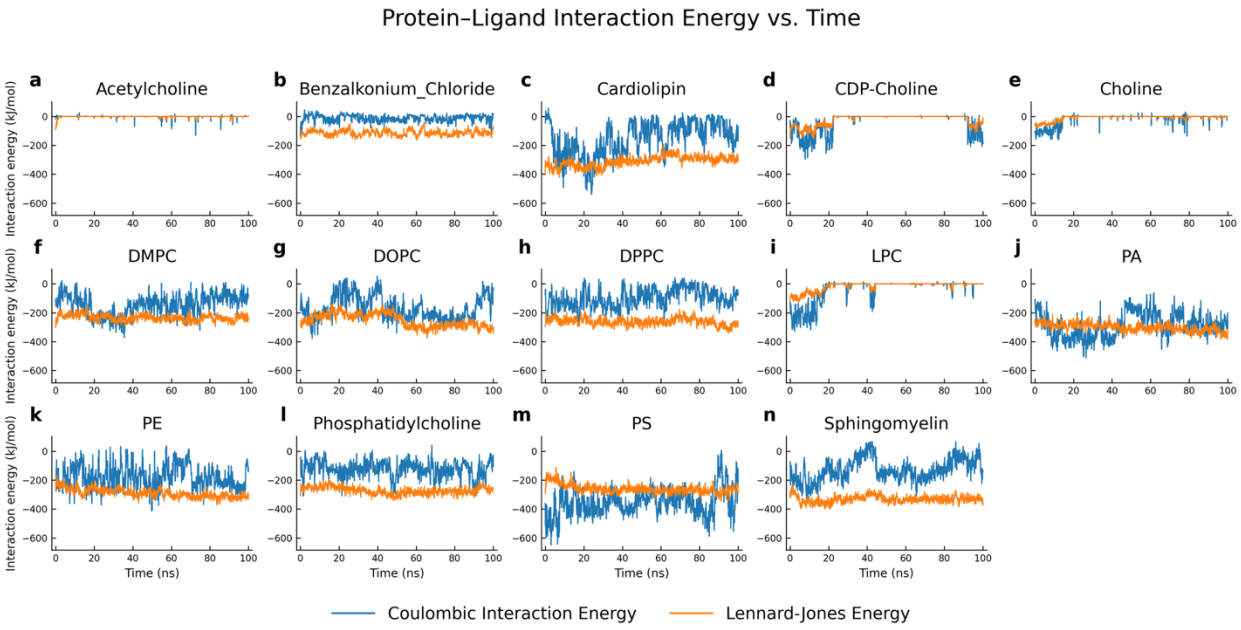

Figure S3. Protein-ligand interaction energies decomposition. The Coulombic (blue) and Lennard-Jones (orange) interaction energies between Human Serum Albumin (HSA) and a) Acetylcholine, b) Benzalkonium Chloride, c) Cardiolipin, d) CDP-Choline, e) Choline, f) Dimyristoylphosphatidylcholine (DMPC), g) Dioleoylphosphatidylcholine (DOPC), h) Dipalmitoylphosphatidylcholine (DPPC), i) Lysophosphatidylcholine (LPC), j) Phosphatidic acid (PA), k) Phosphatidylethanolamine (PE), l) Phosphatidylcholine, m) Phosphatidylserine (PS), and n) Sphingomyelin are shown. Larger negative values indicate stronger interaction energy.

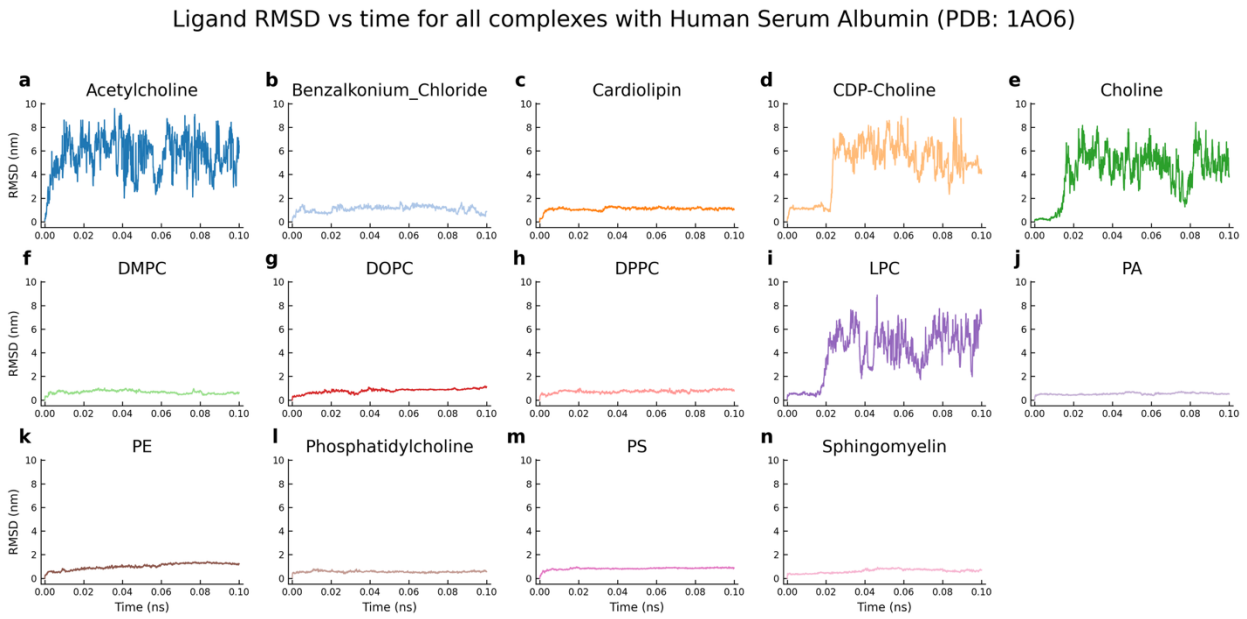

Figure S4. Ligand Root Mean Squared Deviation (RMSD). The RMSD calculations over the simulation time of a) Acetylcholine, b) Benzalkonium Chloride, c) Cardiolipin, d) CDP-Choline, e) Choline, f) Dimyristoylphosphatidylcholine (DMPC), g) Dioleoylphosphatidylcholine (DOPC), h) Dipalmitoylphosphatidylcholine (DPPC), i) Lysophosphatidylcholine (LPC), j) Phosphatidic acid (PA), k) Phosphatidylethanolamine (PE), l) Phosphatidylcholine, m) Phosphatidylserine (PS), and n) Sphingomyelin are shown. RMSD was computed between the ligand heavy atoms and HSA protein backbone structure. Lower RMSD values with stable time-series progression indicate conformationally stable and well bound ligands, while larger RMSD values with unstable fluctuations throughout the simulation indicate dissociations, rearrangement, or complete detachment from the binding site. Acetylecholine, CDP-Choline, Choline, and Lysophosphatidylcholine (LPC) all exhibited weak binding and detachment from the binding site.

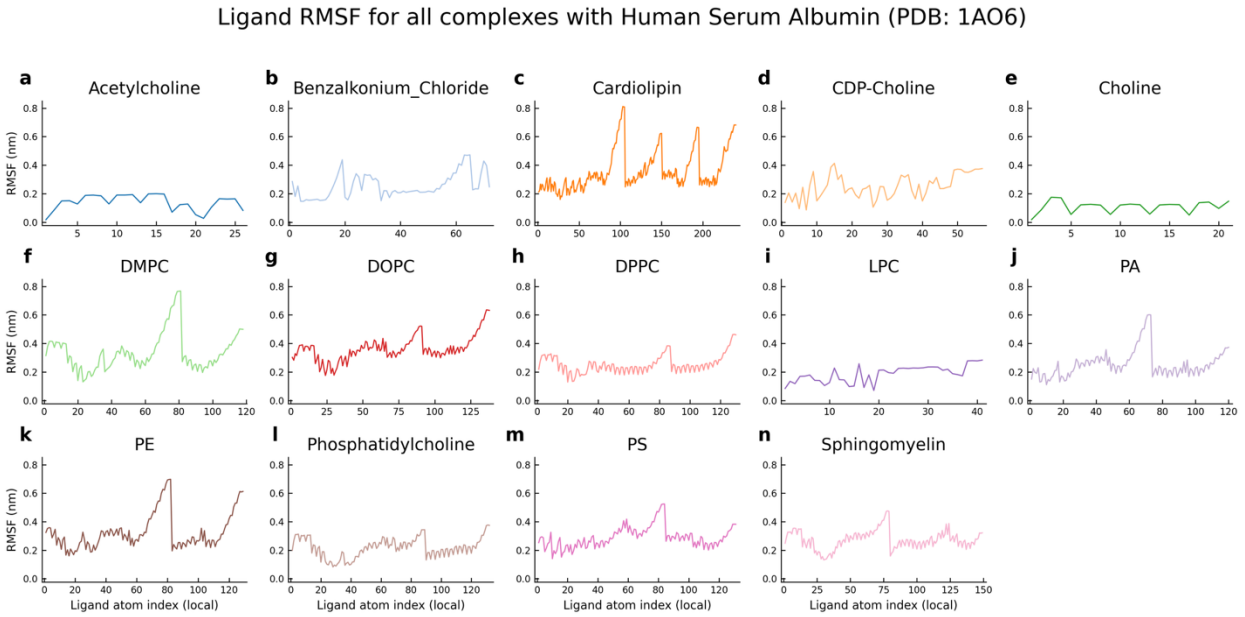

Figure S5. Ligand Root Mean Squared Fluctuation (RMSF). The RMSF calculations of the atomic positions of a) Acetylcholine, b) Benzalkonium Chloride, c) Cardiolipin, d) CDP-Choline, e) Choline, f) Dimyristoylphosphatidylcholine (DMPC), g) Dioleoylphosphatidylcholine (DOPC), h) Dipalmitoylphosphatidylcholine (DPPC), i) Lysophosphatidylcholine (LPC), j) Phosphatidic acid (PA), k) Phosphatidylethanolamine (PE), l) Phosphatidylcholine, m) Phosphatidylserine (PS), and n) Sphingomyelin in the trajectory are shown. Peaks indicate flexible or mobile regions of the ligand within the binding pocket, whereas low RMSF values correspond to more rigid, stably anchored segments.

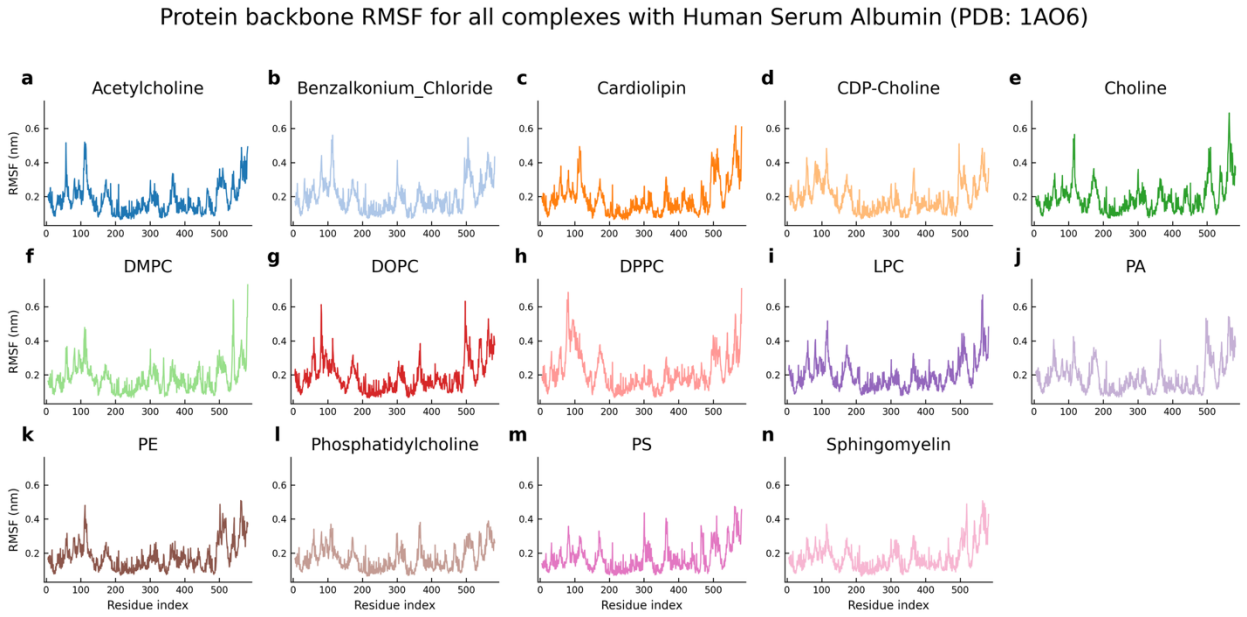

Figure S6. Albumin Root Mean Squared Fluctuation. The RMSF of Human Serum Albumin (HSA) while interacting with a) Acetylcholine, b) Benzalkonium Chloride, c) Cardiolipin, d) CDP-Choline, e) Choline, f) Dimyristoylphosphatidylcholine (DMPC), g) Dioleoylphosphatidylcholine (DOPC), h) Dipalmitoylphosphatidylcholine (DPPC), i) Lysophosphatidylcholine (LPC), j) Phosphatidic acid (PA), k) Phosphatidylethanolamine (PE), l) Phosphatidylcholine, m) Phosphatidylserine (PS), and n) Sphingomyelin is shown. Comparison across panels highlights which regions of HSA are intrinsically flexible and how the presence of different ligands modulates local backbone dynamics, particularly in and around the relevant binding sites.

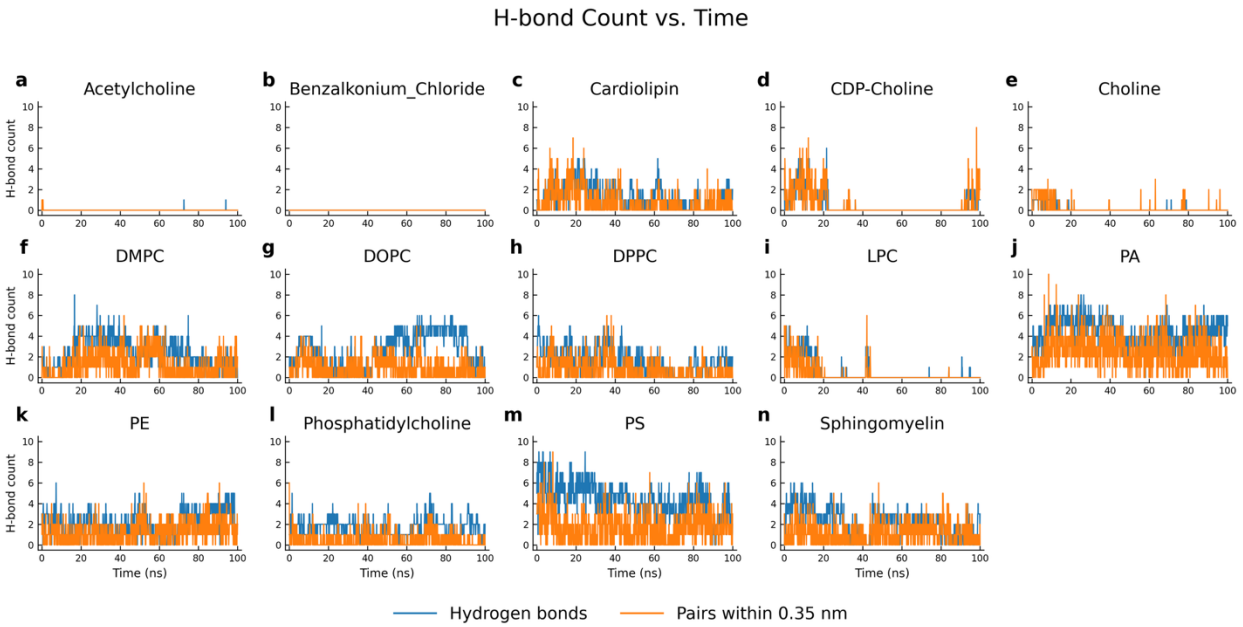

Figure S2. Total Hydrogen-Bonding counts (blue) and counts under 3.5Å (orange) between Human Serum Albumin and a) Acetylcholine, b) Benzalkonium Chloride, c) Cardiolipin, d) CDP-Choline, e) Choline, f) Dimyristoylphosphatidylcholine (DMPC), g) Dioleoylphosphatidylcholine (DOPC), h) Dipalmitoylphosphatidylcholine (DPPC), i) Lysophosphatidylcholine (LPC), j) Phosphatidic acid (PA), k) Phosphatidylethanolamine (PE), l) Phosphatidylcholine, m) Phosphatidylserine (PS), and n) Sphingomyelin over the 100-ns production simulation.

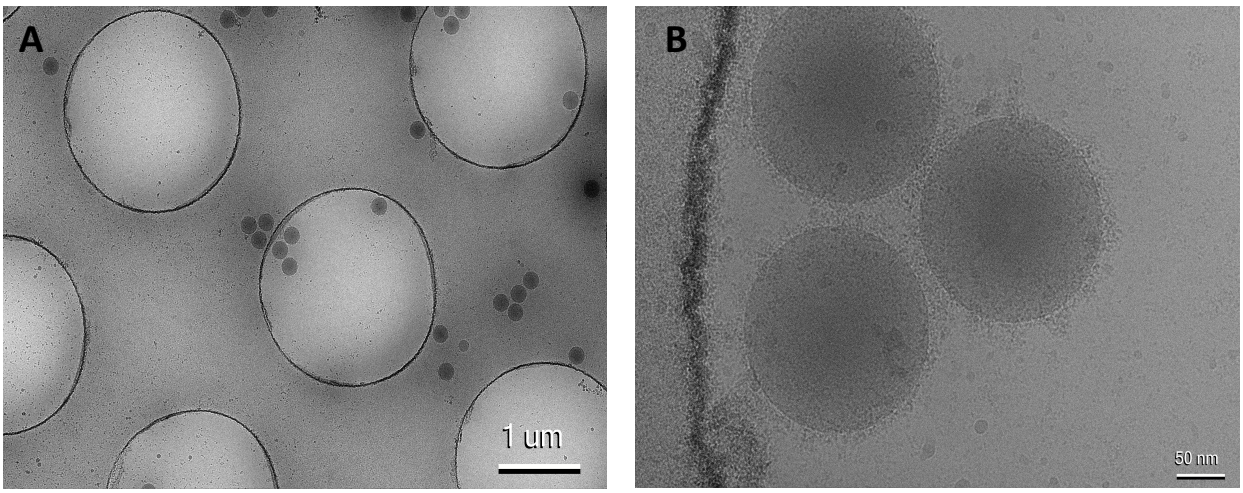

Figure S8. Cryo-TEM images showing the protein corona formed on nanoparticles. Polystyrene nanoparticles were incubated with human plasma in the presence of gold fiducial markers prior to cryo-TEM imaging. Nanoparticles were visualized after formation of the hard protein corona (A) 1 µm and (B) 50 nm. Gold fiducial markers appear as dark dots.

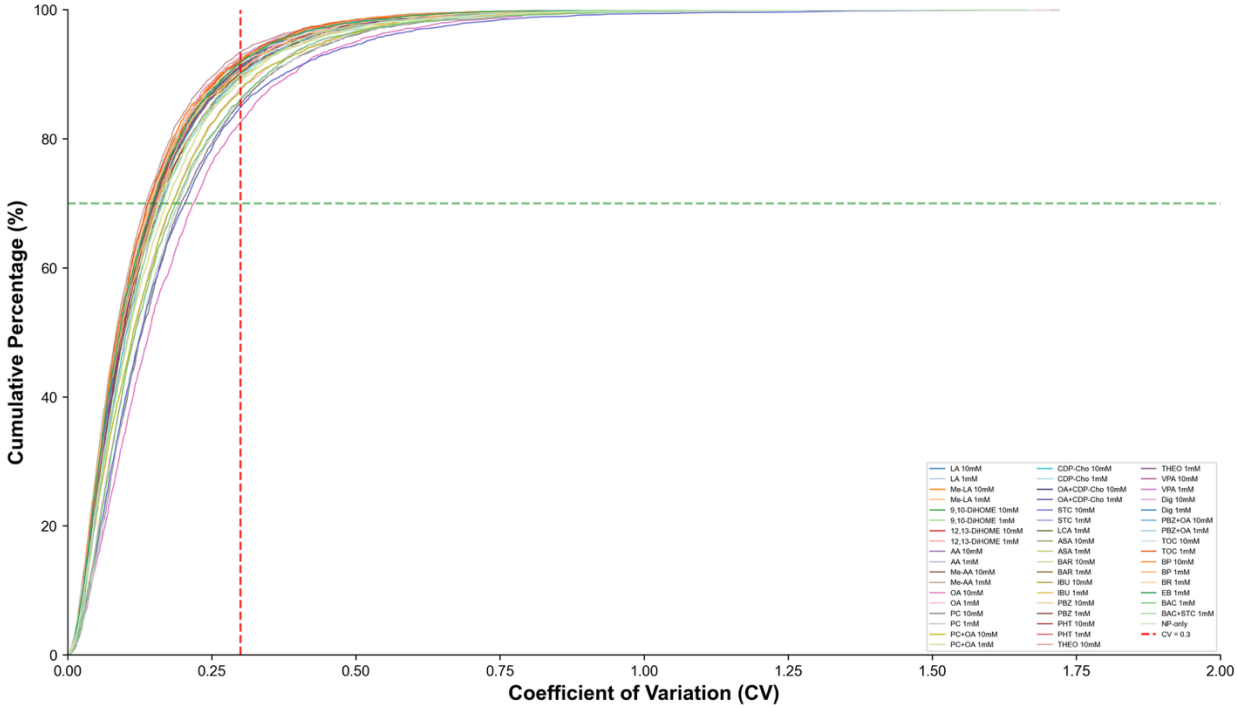

Figure S9. Reproducibility of protein quantification across experimental conditions. Cumulative distribution of the coefficient of variation (CV) for protein abundances calculated across replicate measurements for each tested condition. Each curve represents a different sample condition. The x-axis shows the CV, while the y-axis indicates the cumulative percentage of quantified proteins with CV values below a given threshold. The vertical dashed red line marks a CV of 0.30, a commonly used reproducibility threshold in proteomics, while the horizontal dashed green line indicates the percentage of proteins with CV values below this threshold. The majority of proteins across conditions exhibit CV values below 0.30, indicating high reproducibility of the measurements across replicates.

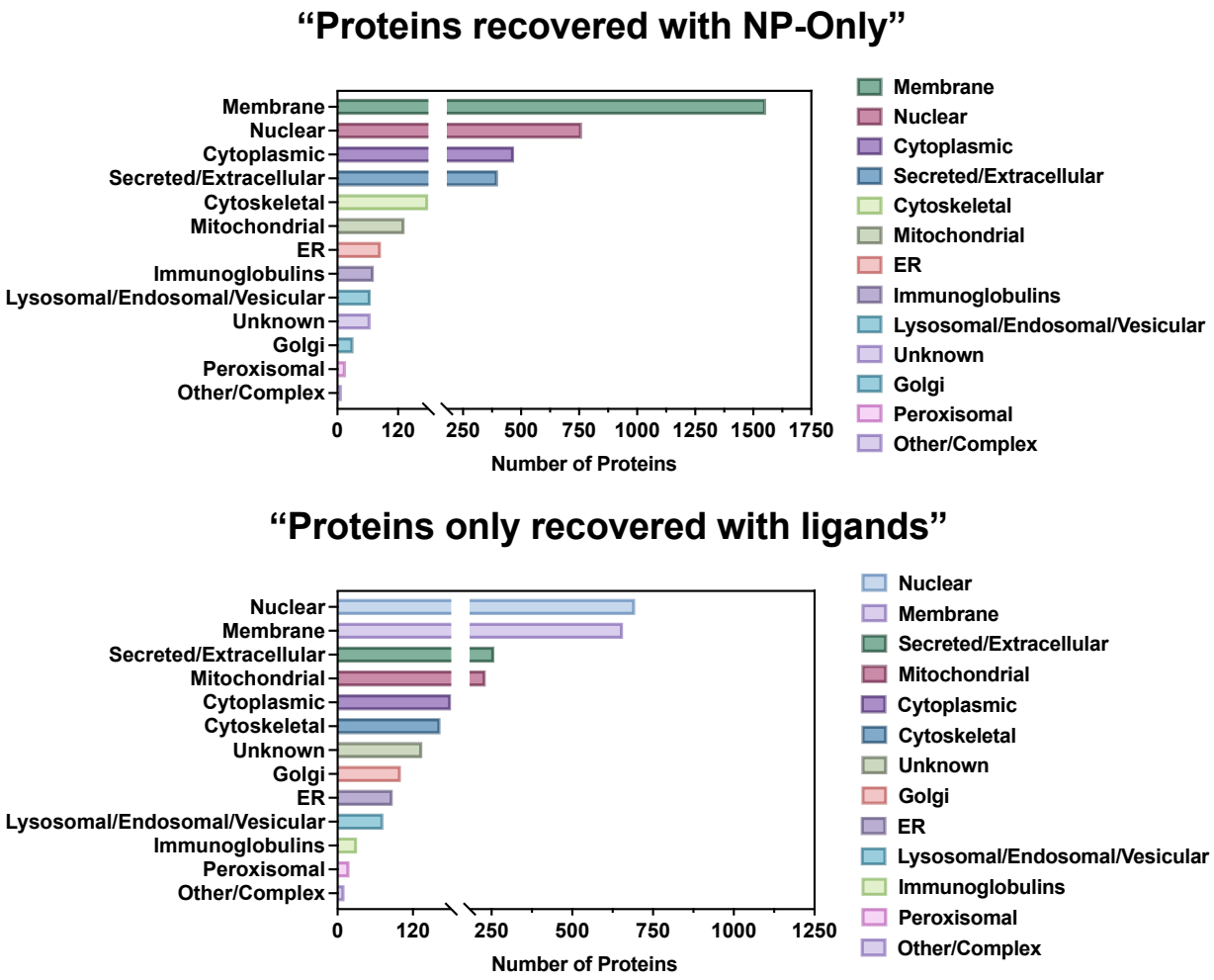

Figure S10. Subcellular location classification of proteins recovered and not recovered with NPs. The left panel shows the distribution of the 3851 proteins recovered with NPs, while the right panel shows the 2646 proteins not recovered with NPs. Proteins were grouped into broad subcellular categories based on annotation, including membrane, nuclear, cytoplasmic, secreted/extracellular, mitochondrial, ER, immunoglobulins, lysosomal/endosomal/vesicular, Golgi, peroxisomal, other/complex, and unknown.

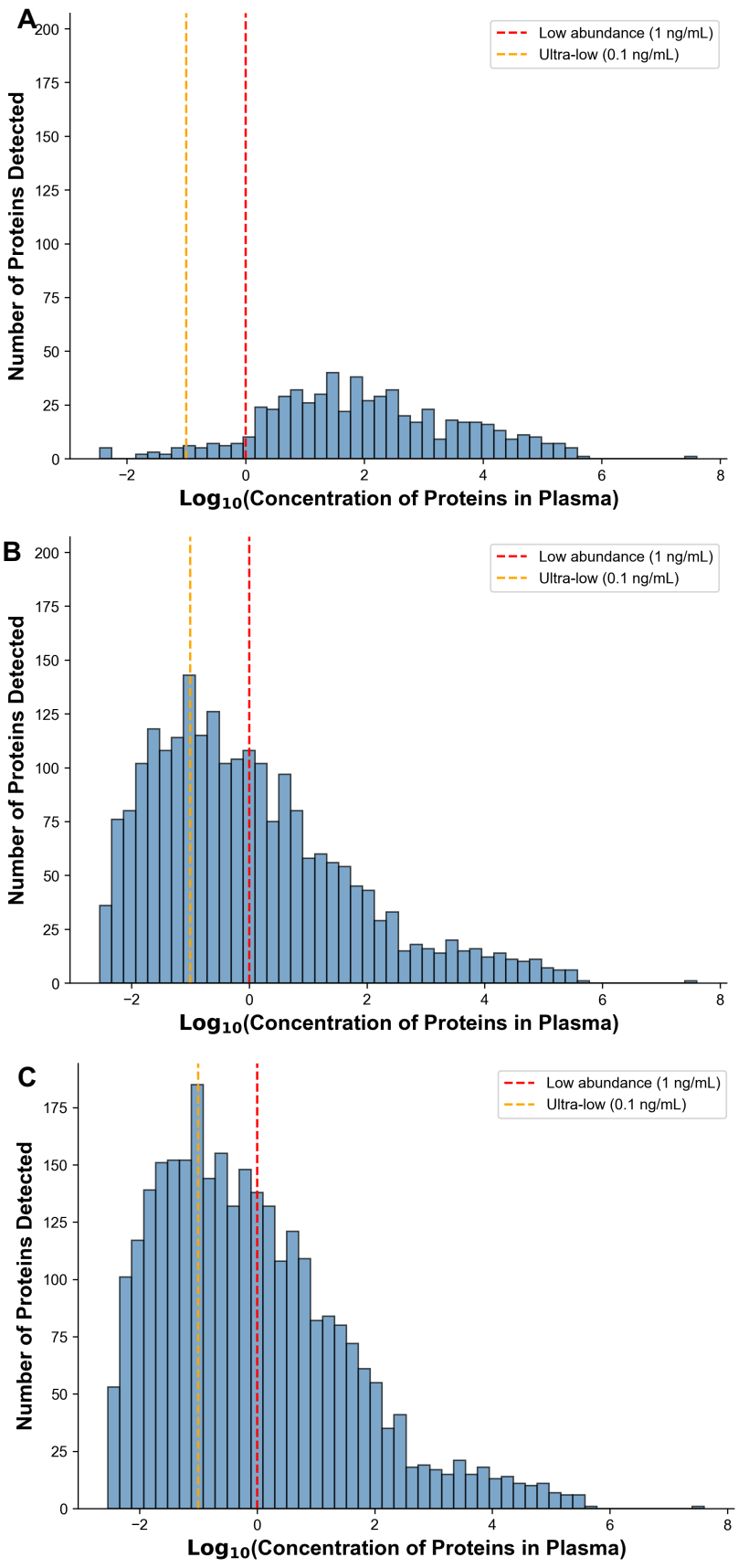
A
B
C
Low abundance (1 ng/mL)
Ultra-low (0.1 ng/mL)
Number of Proteins Detected
Log10(Concentration of Proteins in Plasma)
0
25
50
75
100
125
150
175
200
−2
0
2
4
6
8

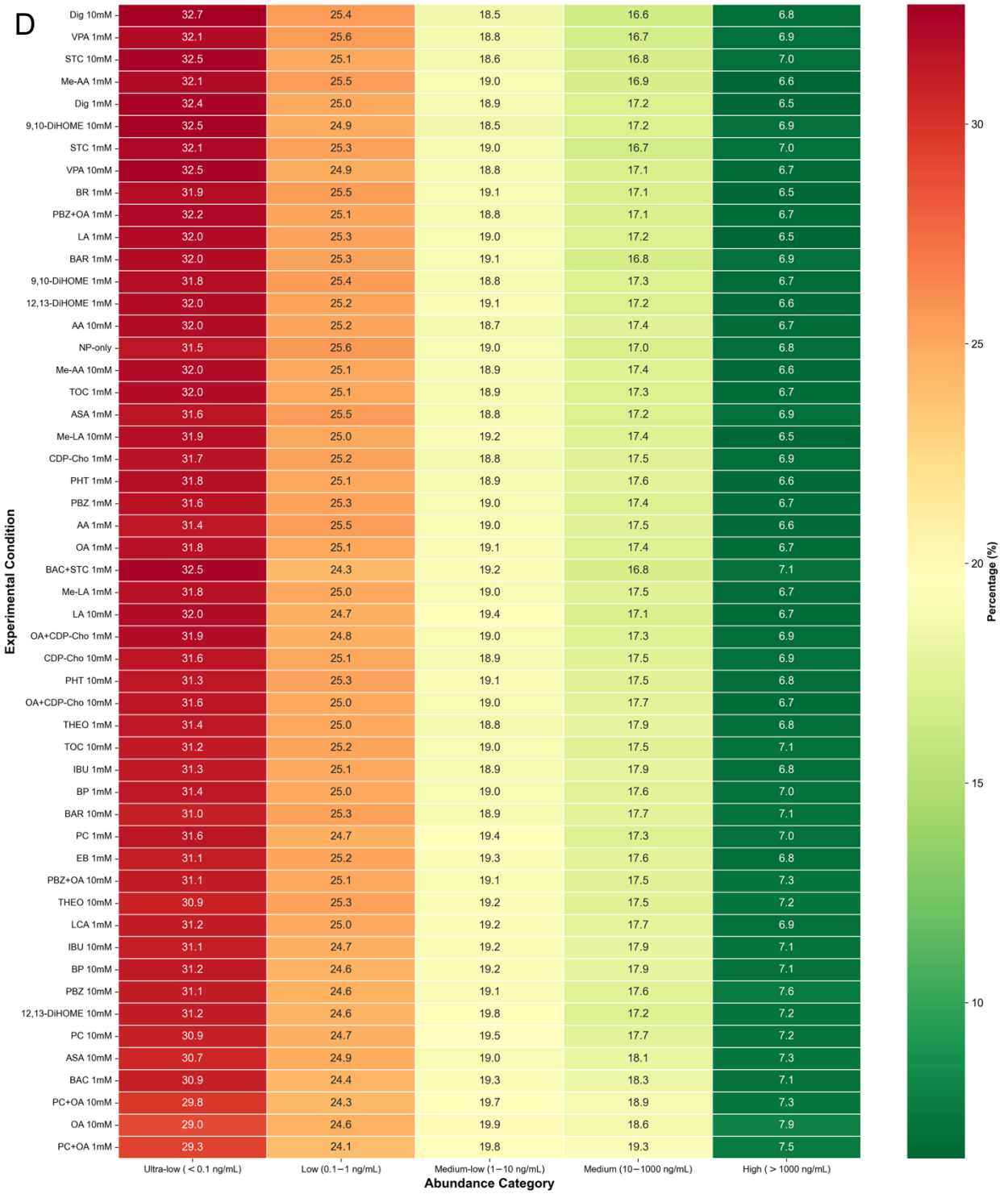

Figure S11. Distribution of detected proteins across plasma abundance ranges and abundance-category enrichment across experimental conditions.[25] Histograms showing the distribution of proteins identified in (A) plasma, (B) NP-only nanoparticle corona samples, and (C) nanoparticle coronas formed in the presence of small-molecule treatments. The x-axis represents the reported plasma concentration of proteins (log_{10} scale), and the y-axis indicates the number of proteins detected. Vertical dashed lines mark

the thresholds used to classify low-abundance (1 ng/mL) and ultra-low-abundance (0.1 ng/mL) proteins. These distributions illustrate the shift toward detection of lower-abundance proteins in nanoparticle corona samples compared with plasma alone. (D) Heatmap depicting the proportional distribution of detected proteins across five plasma concentration tiers for each of the 27 selected small-molecule treatment conditions. Rows represent individual experimental conditions; columns represent protein abundance categories defined by reference plasma concentrations from the Human Protein Atlas (HPA) blood mass spectrometry dataset, supplemented by HPA immunoassay data for proteins lacking MS-derived measurements. Values within each cell indicate the row-normalized percentage of annotated proteins belonging to that abundance tier. Across all conditions, approximately 55–58% of concentration-annotated proteins fall below 1 ng/mL, indicating consistent enrichment of low-abundance plasma proteins by the nanoparticle-based capture approach. Color scale (RdYlGn, reversed) represents percentage per row, where darker red denotes greater proportional representation.

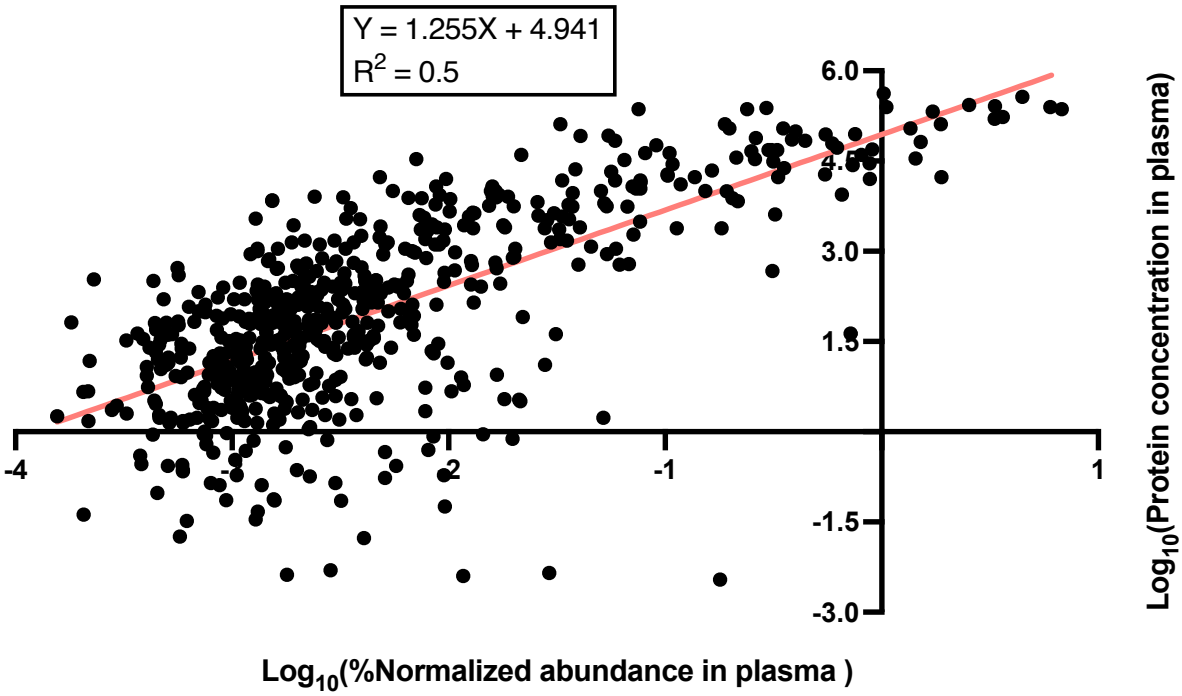

Figure S12. Correlation between protein abundance in plasma and reported plasma protein concentration. The $\log_{10}$-transformed normalized abundance in plasma is plotted against the $\log_{10}$-transformed protein concentration in plasma for the identified proteins. Each dot represents one protein, and the red line shows the linear regression fit.

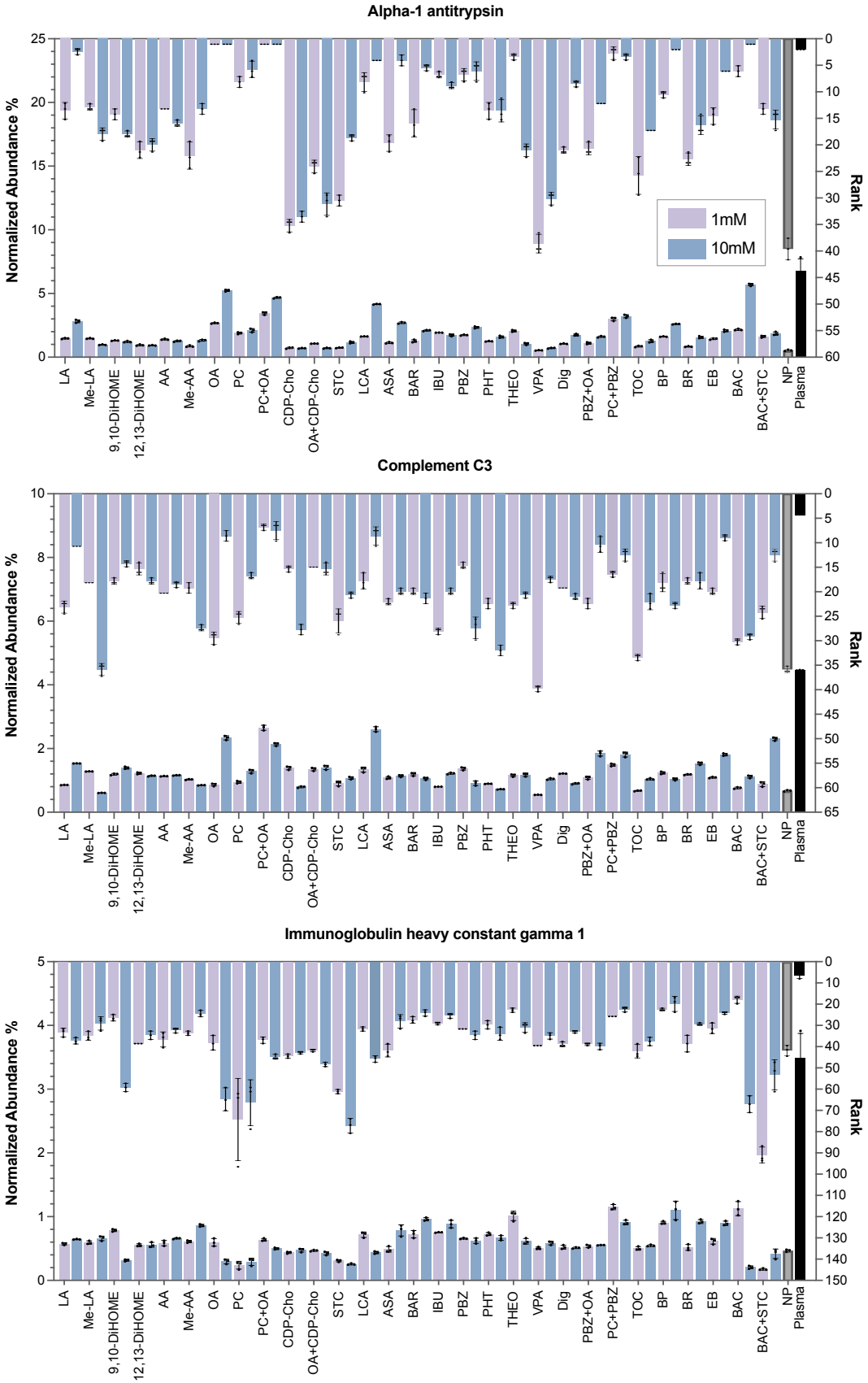
Alpha-1 antitrypsin
Normalized Abundance %
Rank
1mM
10mM
LA
Me-LA
9,10-DiHOME
12,13-DiHOME
AA
Me-AA
OA
PC
PC+OA
CDP-Cho
OA+CDP-Cho
STC
LCA
ASA
BAR
IBU
PBZ
PHT
THEO
VPA
Dig
PBZ+OA
PC+PBZ
TOC
BP
BR
EB
BAC
BAC+STC
NP
Plasma
Complement C3
Normalized Abundance %
Rank
Immunoglobulin heavy constant gamma 1
Normalized Abundance %
Rank

Figure S13. Distribution of the most abundant plasma proteins across conditions. Rank and relative abundance of alpha-1-antitrypsin, complement C3, and immunoglobulin heavy constant gamma 1 across plasma, untreated NP, and small-molecule–treated coronas.

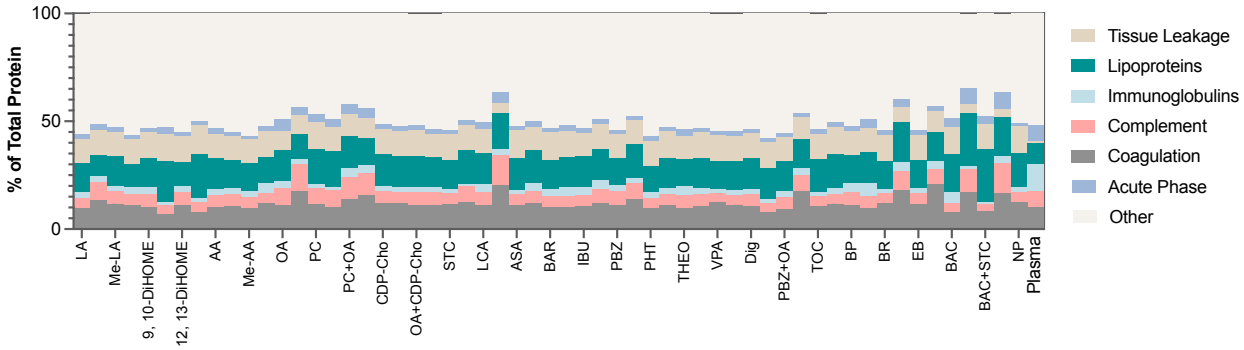

Figure S14. Functional class distribution of proteins identified in NP coronas across experimental conditions. Stacked bar chart showing the relative abundance (% of total protein signal) of major plasma protein functional classes detected in the nanoparticle corona under different small-molecule conditions. Proteins were grouped into six categories: tissue leakage proteins, lipoproteins, immunoglobulins, complement proteins, coagulation proteins, and acute phase proteins, with all remaining proteins classified as "Other." Each bar represents an individual experimental condition, and the height of each colored segment corresponds to the fraction of the total corona composition attributed to that protein class. While the overall corona composition remains dominated by the "Other" category, variations in the relative contributions of lipoproteins, immunoglobulins, complement, coagulation, and acute phase proteins are observed across conditions, indicating that the presence of different small molecules can modulate the functional composition of the protein corona. The 10 mM concentration is followed by the 1 mM concentration for each compound.

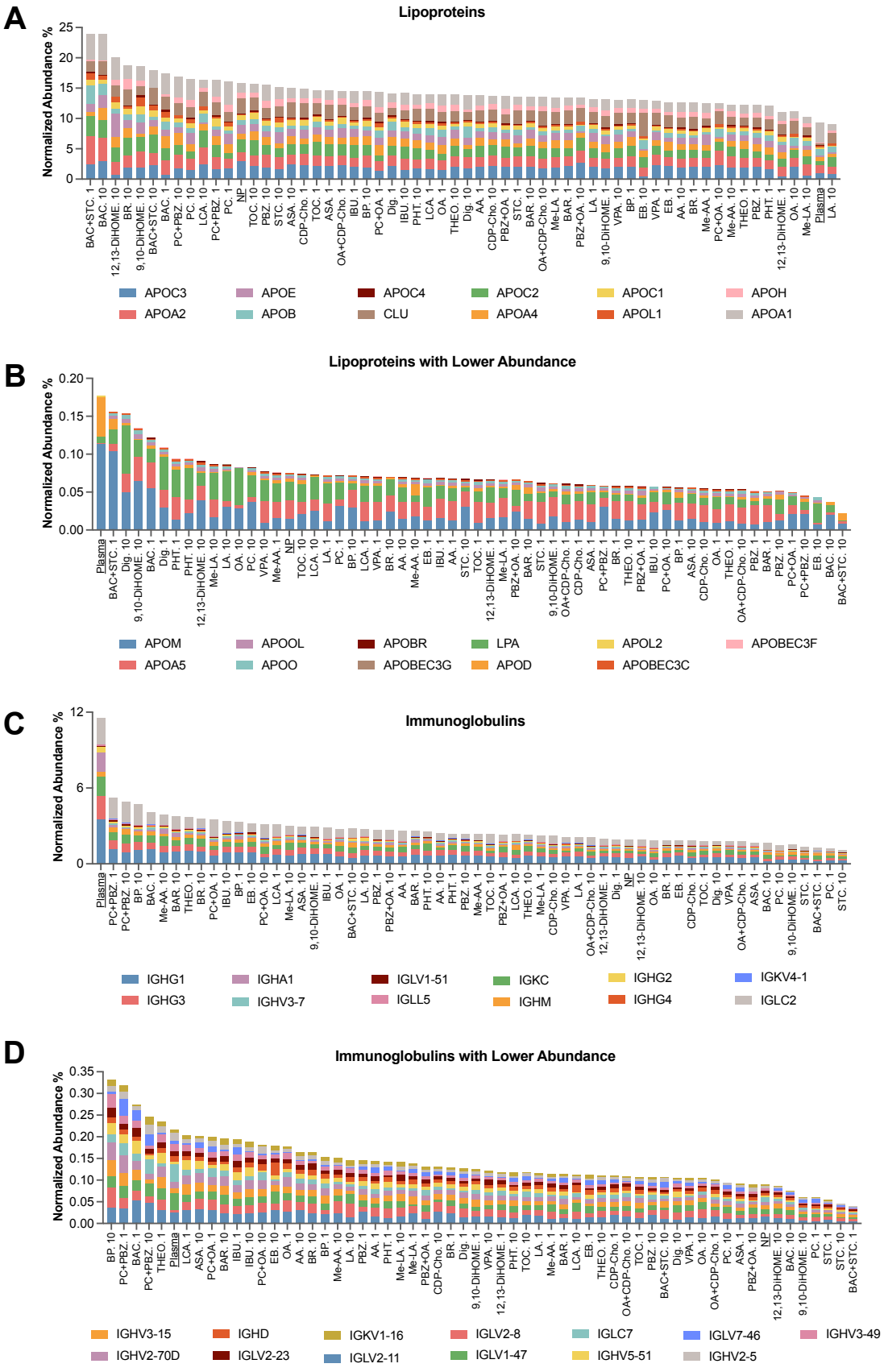
A
Lipoproteins
Normalized Abundance %
APOC3
APOE
APOC4
APOC2
APOC1
APOH
APOA2
APOB
CLU
APOA4
APOL1
APOA1
B
Lipoproteins with Lower Abundance
Normalized Abundance %
APOM
APOOL
APOBR
LPA
APOL2
APOBEC3F
APOA5
APOO
APOBEC3G
APOD
APOBEC3C
C
Immunoglobulins
Normalized Abundance %
IGHG1
IGHA1
IGLV1-51
IGKC
IGHG2
IGKV4-1
IGHG3
IGHV3-7
IGLL5
IGHM
IGHG4
IGLC2
D
Immunoglobulins with Lower Abundance
Normalized Abundance %
IGHV3-15
IGHD
IGKV1-16
IGLV2-8
IGLC7
IGLV7-46
IGHV3-49
IGHV2-70D
IGLV2-23
IGLV2-11
IGLV1-47
IGHV5-51
IGHV2-5

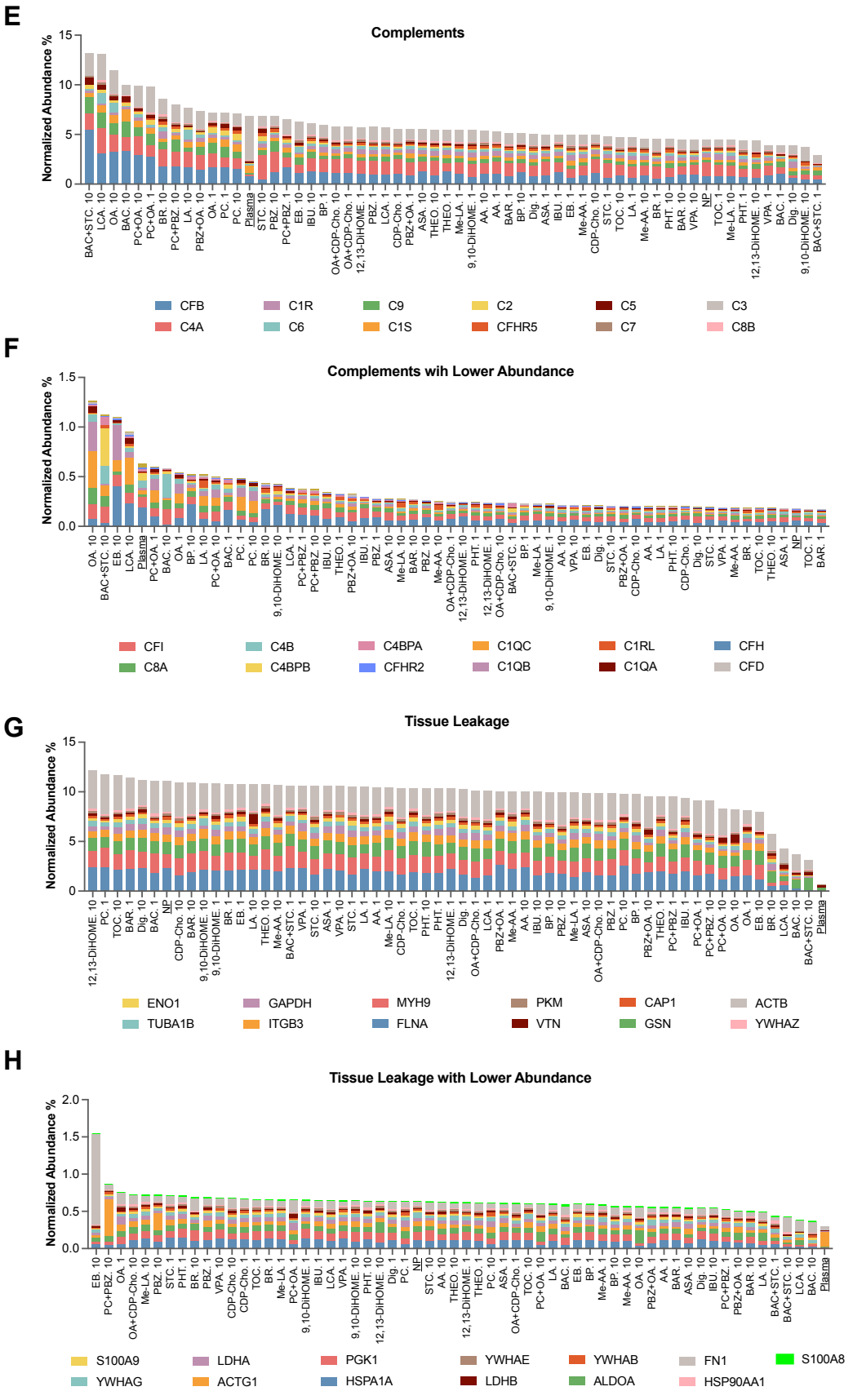
E
Complements
Normalized Abundance %
CFB
C4A
C1R
C6
C9
C1S
C2
CFHR5
C5
C7
C3
C8B
F
Complements wih Lower Abundance
Normalized Abundance %
CFI
C8A
C4B
C4BPB
C4BPA
CFHR2
C1QC
C1QB
C1RL
C1QA
CFH
CFD
G
Tissue Leakage
Normalized Abundance %
ENO1
TUBA1B
GAPDH
ITGB3
MYH9
FLNA
PKM
VTN
CAP1
GSN
ACTB
YWHAZ
H
Tissue Leakage with Lower Abundance
Normalized Abundance %
S100A9
YWHAG
LDHA
ACTG1
PGK1
HSPA1A
YWHAE
LDHB
YWHAB
ALDOA
FN1
HSP90AA1
S100A8

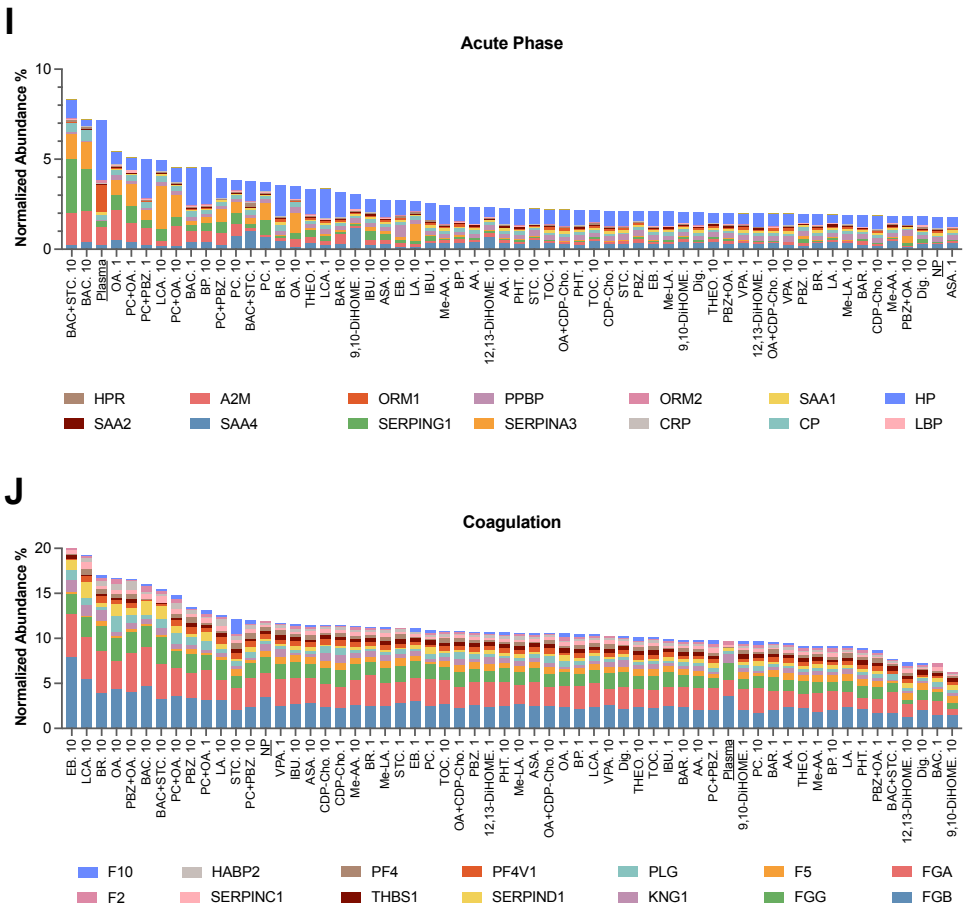

Figure S15. Distribution of individual proteins within major plasma protein classes across experimental conditions. Stacked bar charts showing the normalized abundance (%) of individual proteins within each functional class identified in the nanoparticle corona across all tested conditions. Each bar represents one experimental condition, and colored segments correspond to individual proteins belonging to the indicated class. (A) and (B) Lipoprotein-associated proteins; (C) and (D) Immunoglobulin proteins; (E) and (F) Complement system proteins; (G) and (H) Tissue leakage proteins; (I) Acute phase proteins; and (J) Coagulation-related proteins.

Heatmap of Lipoproteins (A)

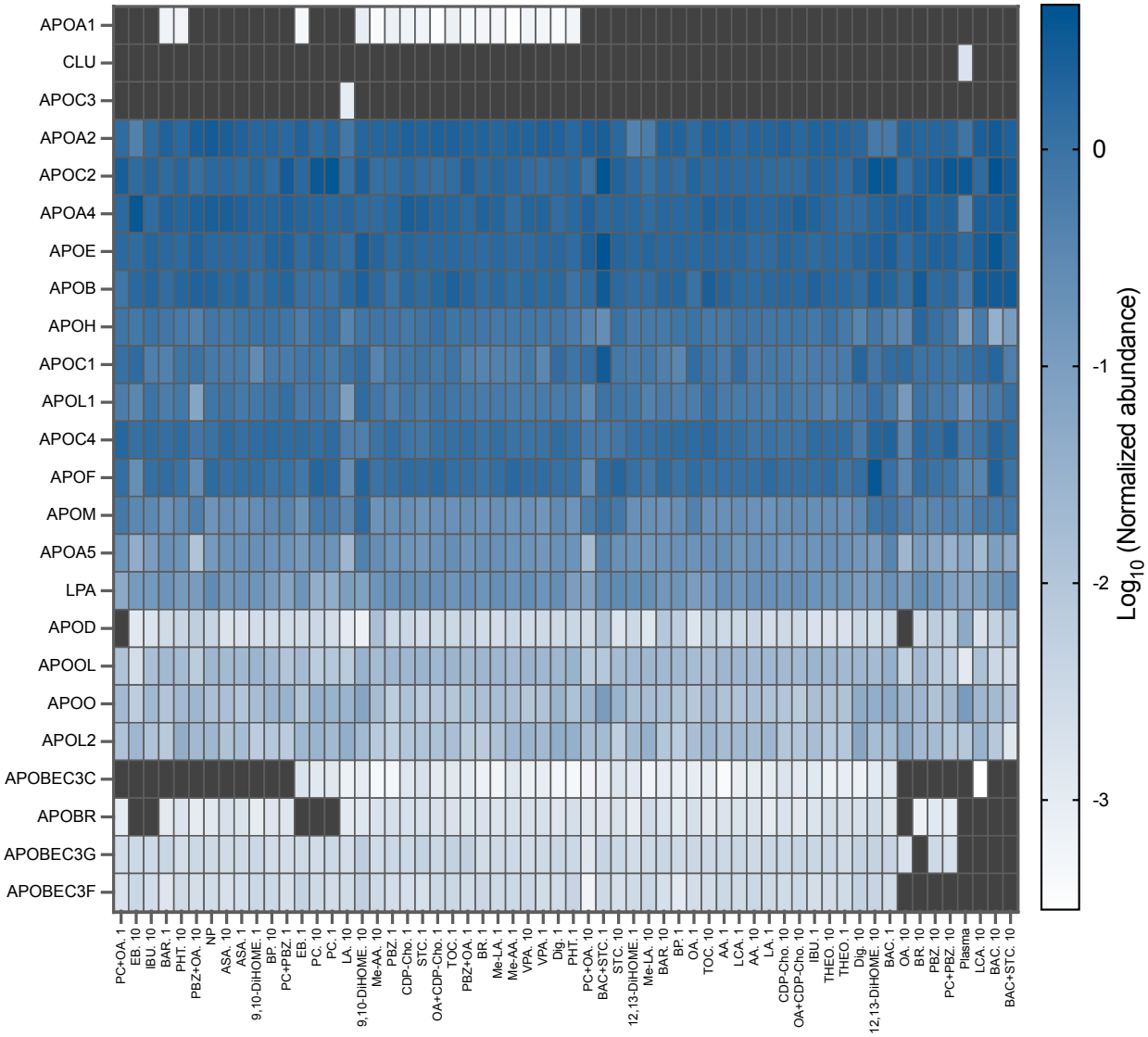

Heatmap of Immunoglobulins (B)

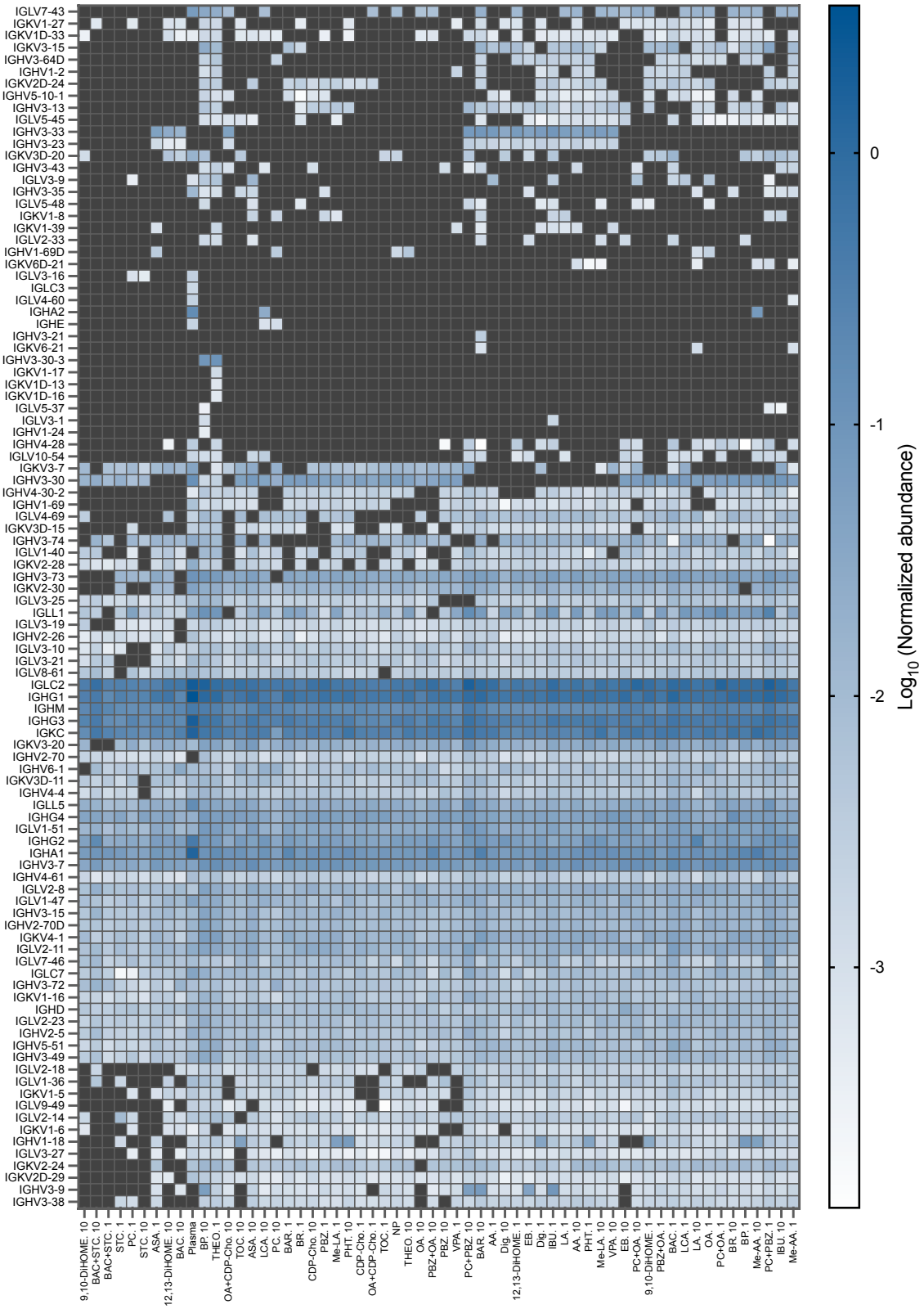

Heatmap of Coagulation Proteins (C)

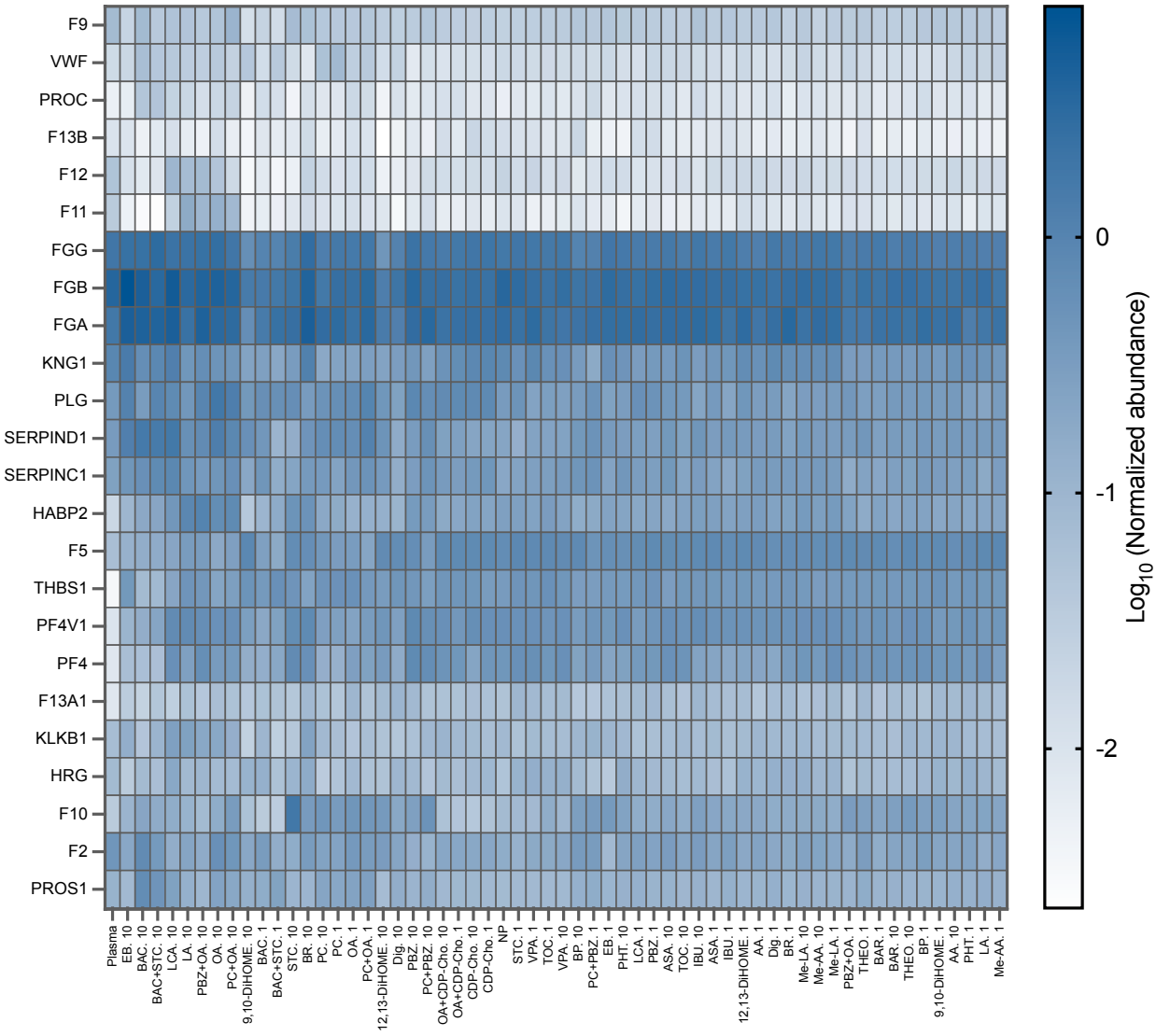

Heatmap of Acute Phase Proteins (D)

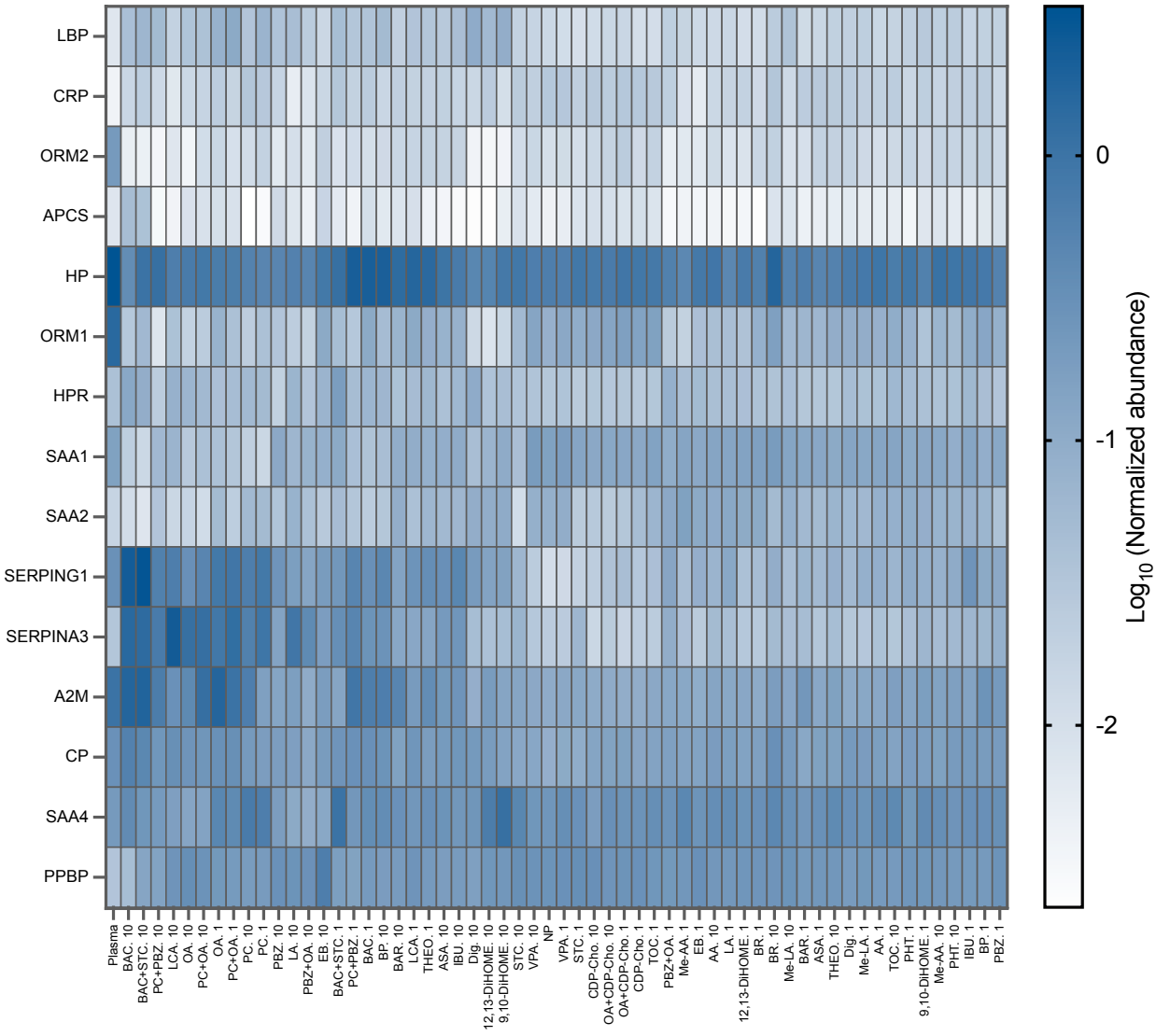

Heatmap of Complements (E)

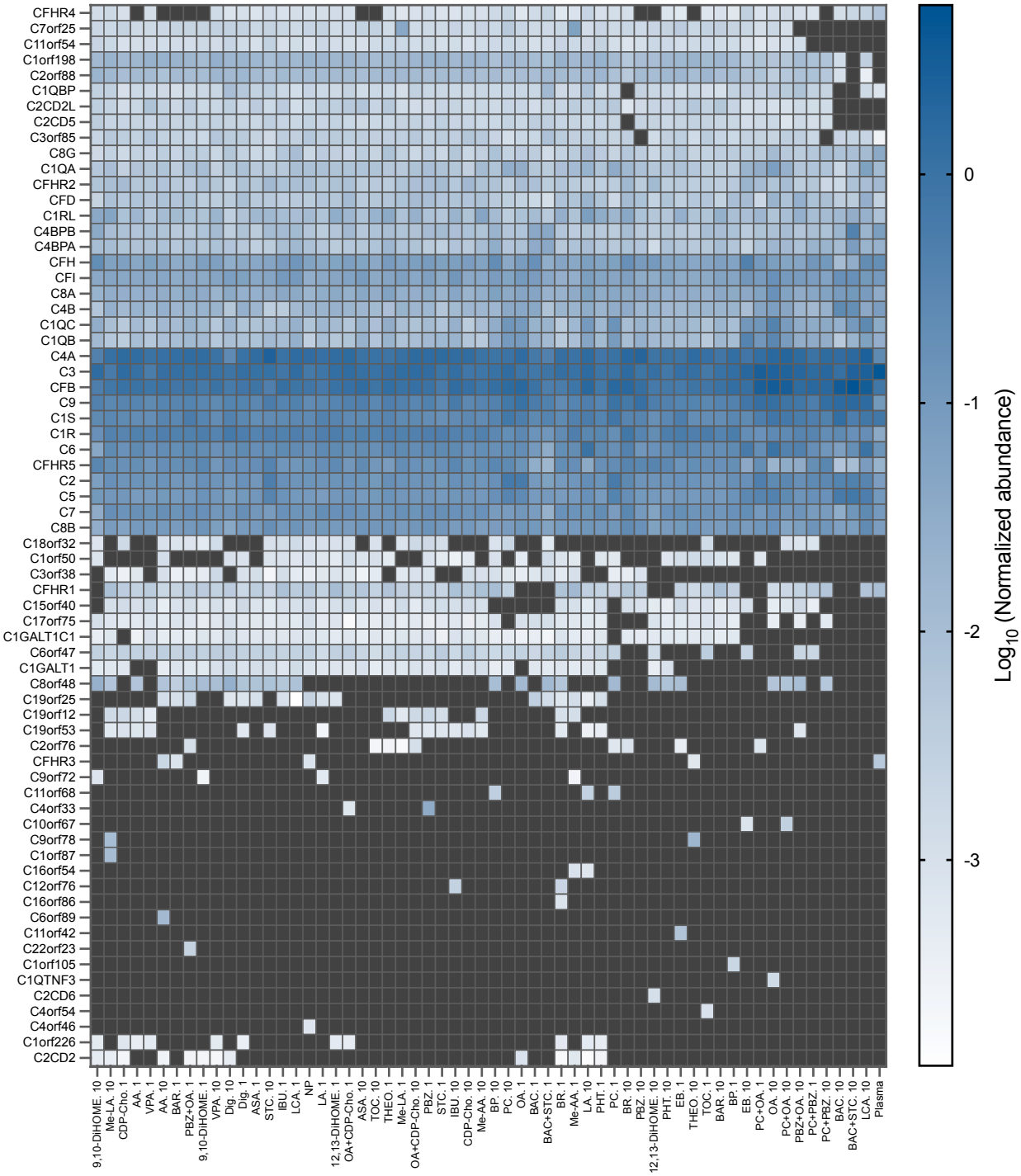

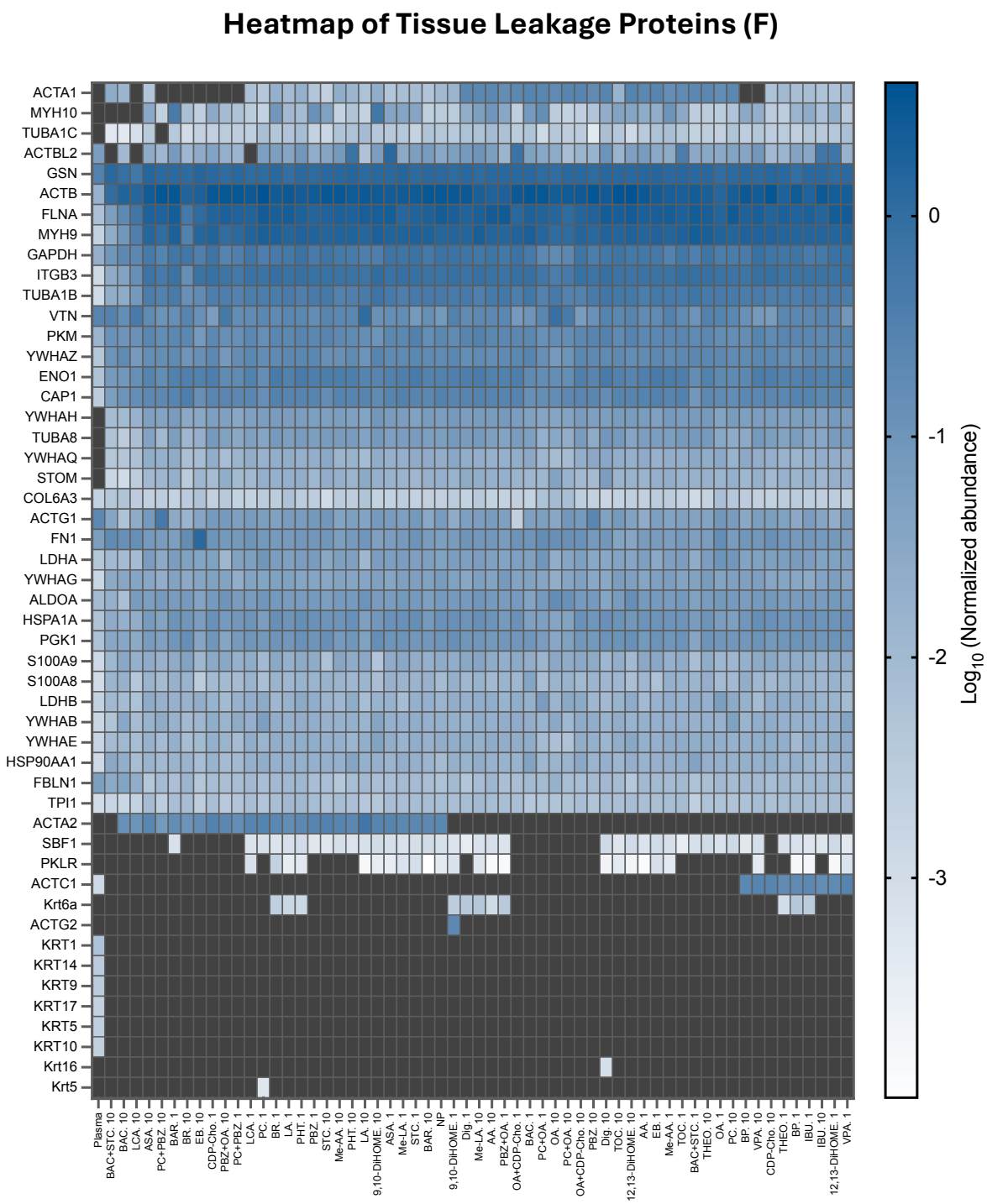

Figure S16. Heatmaps showing the relative abundance of (A) lipoproteins, (B) immunoglobulins, (C) coagulation proteins, (D) acute phase proteins, (E) complements, (F) tissue leakage proteins across all tested conditions. Rows represent individual proteins and columns represent the different sample conditions. Color intensity indicates $\log_{10}$-transformed normalized abundance, with darker blue corresponding to higher abundance. Proteins marked with dark gray were not identified in the corresponding condition.

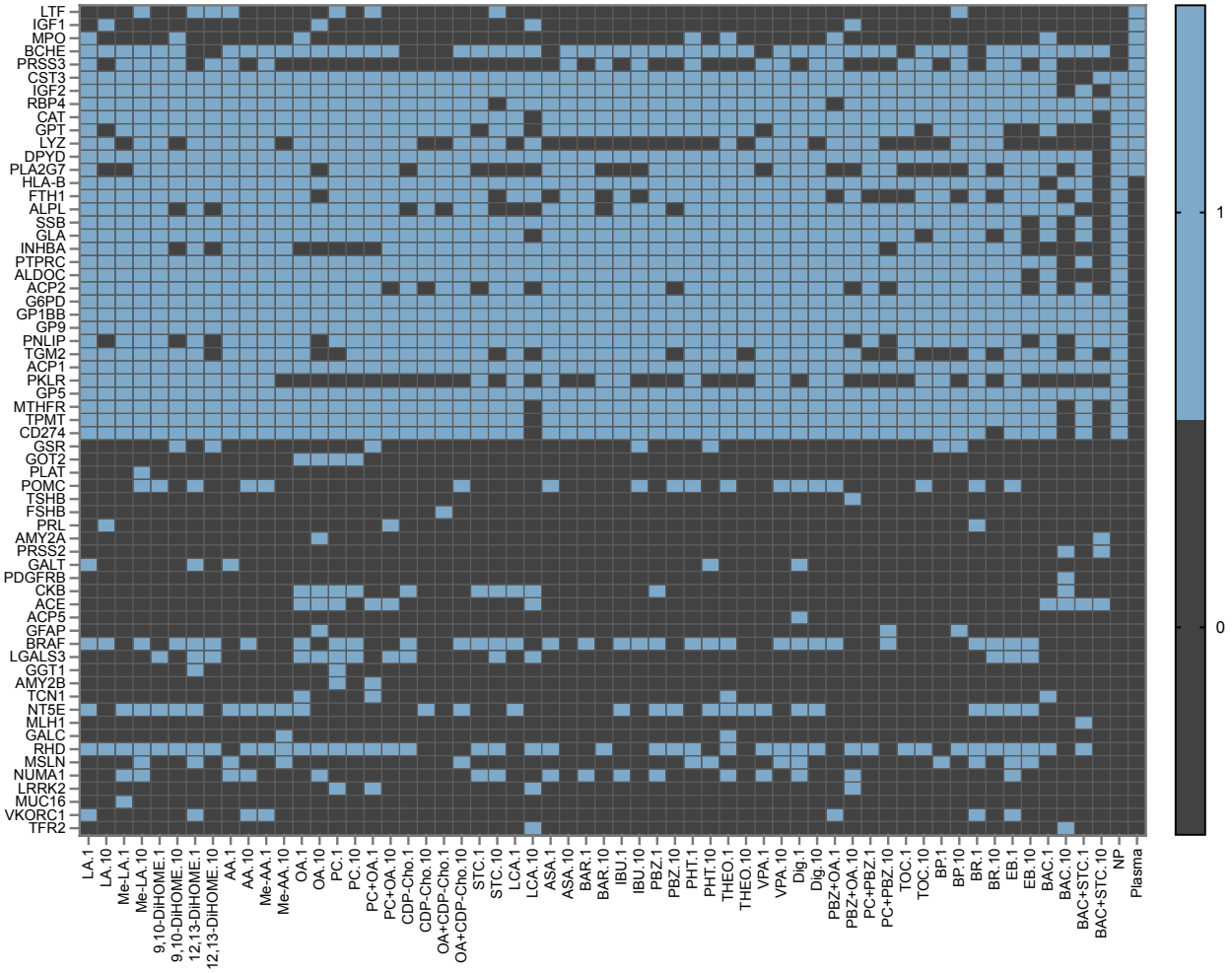

Figure S17. Presence–absence heatmap of FDA biomarkers across experimental conditions. Heatmap showing the detection of selected low-abundance proteins across all tested nanoparticle corona conditions. Rows represent individual proteins and columns correspond to experimental conditions. Light-colored squares indicate the presence (detection) of a protein in a given sample, while dark squares indicate its absence. The color scale represents binary detection values (1 = detected, 0 = not detected).

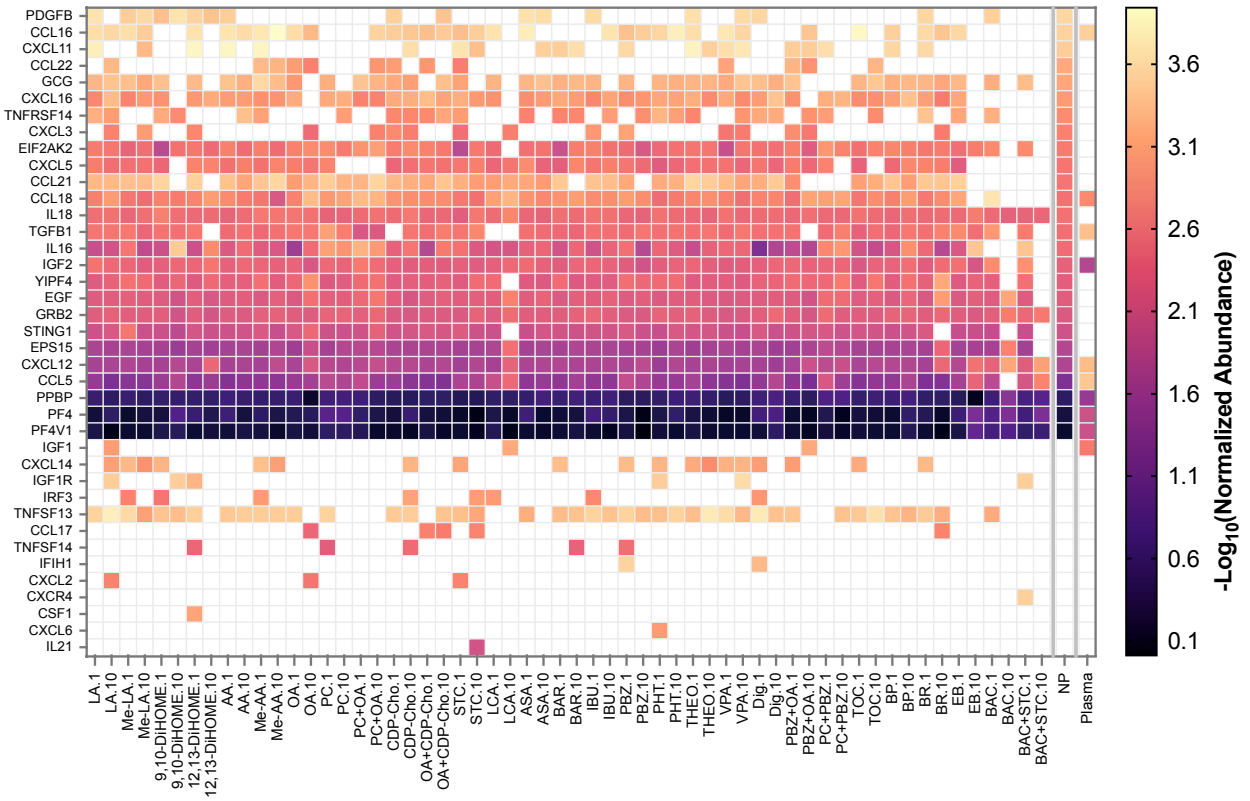

Figure S18. Heatmap of cytokine-related proteins detected across different experimental conditions. Heatmap showing the -$\log_{10}$-transformed normalized abundance of cytokine-related proteins identified in the nanoparticle protein corona formed under different experimental conditions. Each column represents an experimental condition, and each row corresponds to a cytokine-associated protein. Colors indicate the relative normalized abundance of each protein across conditions, with lighter colors representing higher abundance and darker colors indicating lower abundance. Missing values indicate proteins that were not detected in the corresponding sample. The plasma sample is shown as a reference condition.

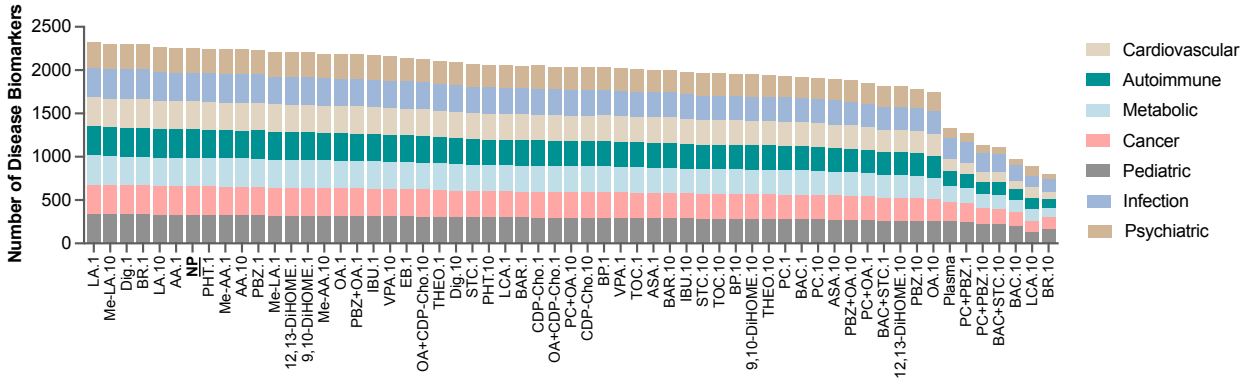

Figure S19. Disease biomarker distribution across conditions. Disease-specific biomarkers are identified based on the HPA (HPA blood PEA atlas, p-adjusted < 0.05 vs. healthy controls).

References

1. Sugio, S., Kashima, A., Mochizuki, S., Noda, M. & Kobayashi, K. Crystal structure of human serum albumin at 2.5 A resolution. Protein engineering 12, (1999).

2. PubChem. 1,2-Dipalmitoylphosphatidylcholine. https://pubchem.ncbi.nlm.nih.gov/compound/6138.

3. PubChem. Dimyristoylphosphatidylcholine, DL-.https://pubchem.ncbi.nlm.nih.gov/compound/26197.

4. PubChem. Phosphatidylethanolamine(PE).https://pubchem.ncbi.nlm.nih.gov/compound/14238554.

5. PubChem. Phosphatidylserines. https://pubchem.ncbi.nlm.nih.gov/compound/9547096.

6. PubChem. 1-18:1-2-18:3-Phosphatidate.https://pubchem.ncbi.nlm.nih.gov/compound/102515448.

7. PubChem. SM(d18:1/24:1(15Z)). https://pubchem.ncbi.nlm.nih.gov/compound/44260126.

8. PubChem. Choline. https://pubchem.ncbi.nlm.nih.gov/compound/305.

9. PubChem. Acetylcholine. https://pubchem.ncbi.nlm.nih.gov/compound/187.

10. PubChem. Lysophosphatidylcholines.https://pubchem.ncbi.nlm.nih.gov/compound/5311264.

11. PubChem.Disodium;[3-[2,3-di(octadeca-9,12-dienoyloxy)propoxy-oxidophosphoryl]oxy-2-hydroxypropyl] 2,3-di(octadeca-9,12-dienoyloxy)propyl phosphate. https://pubchem.ncbi.nlm.nih.gov/compound/75228679.

12. O'Boyle, N. M. et al. Open Babel: An open chemical toolbox. J Cheminform 3, 33 (2011).

13. Eberhardt, J., Santos-Martins, D., Tillack, A. F. & Forli, S. AutoDock Vina 1.2.0: New Docking Methods, Expanded Force Field, and Python Bindings. J Chem Inf Model 61, 3891–3898 (2021).

14. Trott, O. & Olson, A. J. AutoDock Vina: improving the speed and accuracy of docking with a new scoring function, efficient optimization, and multithreading. J Comput Chem 31, 455–461 (2010).

15. Best, R. B. et al. Optimization of the additive CHARMM all-atom protein force field targeting improved sampling of the backbone ϕ, ψ and side-chain χ(1) and χ(2) dihedral angles. J Chem Theory Comput 8, 3257–3273 (2012).

16. Jo, S., Kim, T., Iyer, V. G. & Im, W. CHARMM-GUI: a web-based graphical user interface for CHARMM. J Comput Chem 29, 1859–1865 (2008).

17. Kim, S. et al. CHARMM-GUI ligand reader and modeler for CHARMM force field generation of small molecules. J Comput Chem 38, 1879–1886 (2017).

18. Vanommeslaeghe, K. et al. CHARMM general force field: A force field for drug-like molecules compatible with the CHARMM all-atom additive biological force fields. J Comput Chem 31, 671–690 (2010).

19. Vanommeslaeghe, K. & MacKerell, A. D., Jr. Automation of the CHARMM General Force Field (CGenFF) I: bond perception and atom typing. J Chem Inf Model 52, 3144–3154(2012).

20. Vanommeslaeghe, K., Raman, E. P. & MacKerell, A. D., Jr. Automation of the CHARMM General Force Field (CGenFF) II: assignment of bonded parameters and partial atomic charges. J Chem Inf Model 52, 3155–3168 (2012).

21. Kumar, A., Yoluk, O. & MacKerell, A. D. FFParam: Standalone package for CHARMM additive and Drude polarizable force field parametrization of small molecules. Journal of Computational Chemistry 41, 958–970 (2020).

22. Smith, D. G. A. et al. Psi4 1.4: Open-source software for high-throughput quantum chemistry. J Chem Phys 152, 184108 (2020).

23. Van Der Spoel, D. et al. GROMACS: fast, flexible, and free. J Comput Chem 26, 1701–1718 (2005).

24. Humphrey, W., Dalke, A. & Schulten, K. VMD: visual molecular dynamics. Journal of molecular graphics 14, (1996).

25. Keshavarz, F.; Alavianmehr, M. M.; Yousefi, R., Molecular interaction of benzalkonium Ibuprofenate and its discrete ingredients with human serum albumin. *Physical Chemistry Research* **2013,** *1* (2), 111-116.

26. Timothy J. Boerner, Stephen Deems, Thomas R. Furlani, Shelley L. Knuth, and John Towns. 2023. ACCESS: Advancing Innovation: NSF's Advanced Cyberinfrastructure Coordination Ecosystem: Services & Support. "In Practice and Experience in Advanced Research Computing (PEARC '23)", July 23–27, 2023, Portland, OR, USA. ACM, New York, NY, USA, 4 pages. https://doi.org/10.1145/3569951.3597559

27. San Diego Supercomputer Center (2025): Expanse. University of California San Diego. Service. https://doi.org/10.1145/3437359.3465588